PERGAMON

Journal of Structural Geology 25 (2003) 1623–1644

JOURNAL OF STRUCTURAL GEOLOGY

www.elsevier.com/locate/jsg

Duplex style and triangle zone formation: insights from physical modeling

Brent A. Couzens-Schultz[a,*], Bruno C. Vendeville[b], David V. Wiltschko[c]

[a]*Shell International Exploration and Production, Inc. P.O. Box 481, Houston, TX 77001, USA*
[b]*Bureau of Economic Geology, The University of Texas at Austin, University Station, Box X, Austin, TX 78713, USA*
[c]*Department of Geology and Geophysics, Texas A&M University, College Station, TX 77843, USA*

Received 23 December 2001; received in revised form 23 September 2002; accepted 12 December 2002

Abstract

Duplexes are a common feature in thrust belts at many scales. Their geometries vary significantly from antiformal stacks with significant forethrusting in the cover (e.g. southern Pyrennes, Spain) to triangle zones (e.g. foreland Canadian Rockies) to low-displacement individually spaced ramp-anticlines (e.g. Sub-Andean thrust belt, Bolivia). We present a series of physical experiments demonstrating that the strength of the décollements relative to that of the intervening and overlying rock layers plays a significant role in controlling the duplex style. The models comprise brittle layers made of dry quartz sand and décollements made of two types of viscous silicone polymers. The strength of the décollements in the models is a function of the shortening rate applied to the model. The relative strength of the décollements and surrounding rocks affects the development of active- or passive-roof duplexes (triangle zones). It also affects the amount of translation of individual thrust blocks and the spacing of thrust ramps, which in turn determine if a duplex evolves into an antiformal stack or into individually spaced ramp-anticlines. Model results indicate that specific associations of structural features form systematically under similar rheological and boundary conditions. The presence of relatively strong décollements promotes local underthrusting of the cover, individual ramp-anticlines, internal deformation of thrust sheets, low early layer-parallel shortening, and sequential towards-the-foreland propagation of structures. Weak décollements promote forethrusting of the cover, antiformal stacks, coeval growth of structures, and low internal strain, with the exception of significant early layer-parallel shortening. No underthrusting at a regional scale occurred in any model.
© 2003 Elsevier Science Ltd. All rights reserved.

Keywords: Duplex style; Triangle zone formation; Antiformal stacks

1. Introduction

The causes of the variations in thrust belt style have long been a subject of interest. As early as 1892, Bailey Willis noted that even in a single thrust belt, such as the Appalachians, a variety of different structures develop despite having been subjected to a similar compressional regime. Willis (1892) suggested that stratigraphic variations between or within foldbelts might be responsible for such differences. Since Willis' work, much progress has been made in understanding the mechanical role of stratigraphy on the deformation style. We now know that many thrust belts have more than one décollement, whose location and extent are controlled by stratigraphy (e.g. Williams and Dixon, 1985; Woodward, 1985; Banks and Warburton, 1986; Price, 1986; Vergés and Martínez, 1988, etc.). The presence of multiple décollements commonly leads to duplex formation. In its most basic form, a duplex consists of thrust horses bound by roof and floor décollements overlaying a sequence of cover rocks (e.g. Boyer and Elliott, 1982; McClay, 1992). Fig. 1 illustrates several different duplex geometries in thrust belts and emphasizes the wide variability in style that is possible.

Despite the abundance of duplexes within thrust belts, several questions remain relating to their formation:

1. What causes the different mechanical, and hence deformational, responses of the cover? Why do some duplexes deform by underthrusting and triangle zone formation while others merely transfer shortening to structures in the foreland (compare Fig. 1b, c and i with Fig. 1e, f and g; Fig. 2)?
2. Why have some horse blocks (lower-tier thrust sheets) undergone large translations whereas others have not not (compare Fig. 1e, f, g with Fig. 1a, b and i)?

* Corresponding author. Tel.: +713-245-7707.
E-mail address: brent.couzens@shell.com (B.A. Couzens-Schultz).

0191-8141/03/$ - see front matter © 2003 Elsevier Science Ltd. All rights reserved.
doi:10.1016/S0191-8141(03)00004-X

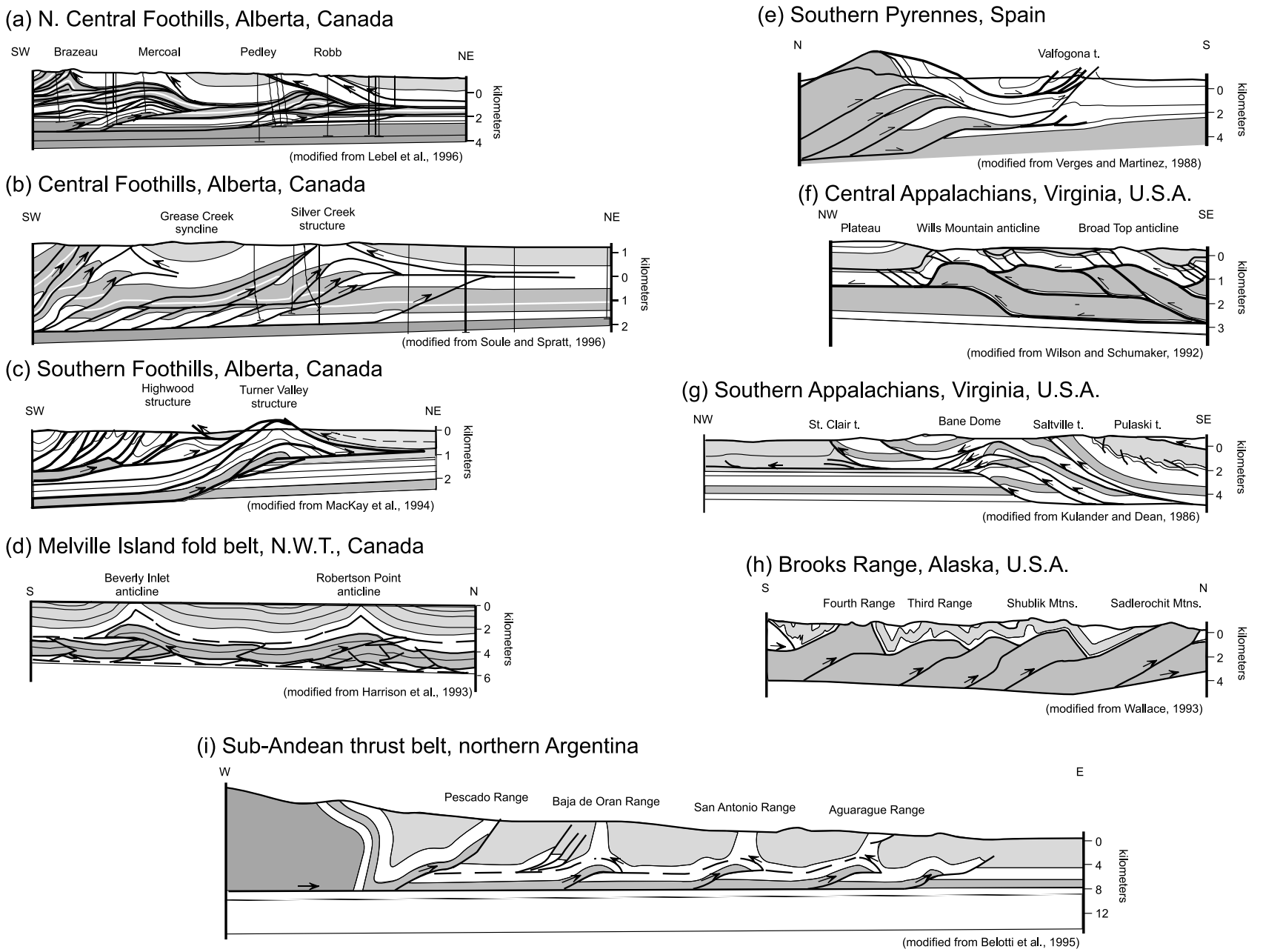

Fig. 1. Examples of duplexes in thrust belts. a–i modified from Lebel et al., 1996; Soule and Spratt, 1996; MacKay et al., 1994; Harrison, 1993; Vergés and Martínez, 1988; Wilson and Shumaker, 1992; Kulander and Dean, 1986; Wallace, 1993 and Belotti et al., 1995 respectively.

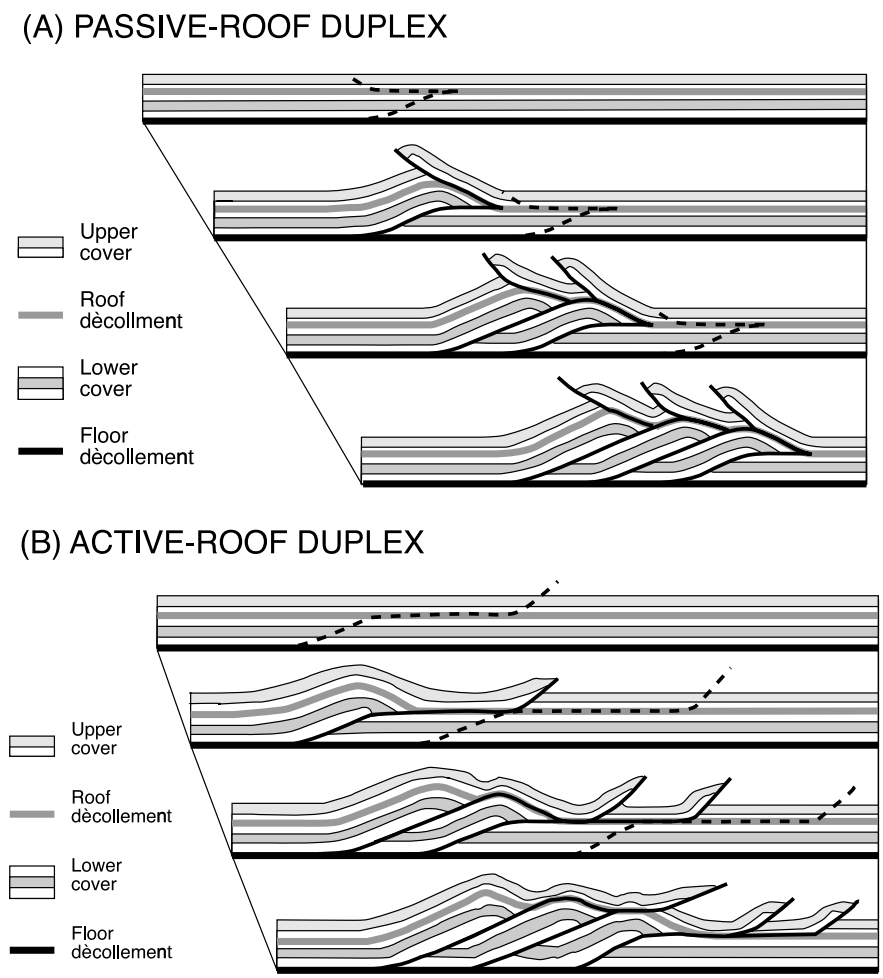

Fig. 2. Possible end-member relationships between cover displacement and horse block displacement. (A) Passive-roof duplex (Banks and Warburton, 1986), where the cover is underthrusted by the horse blocks. (B) Active-roof duplex, where the cover is bulldozed forward by the horse blocks.

3. What controls ramp spacing (compare Fig. 1i and b)?
4. Why do some duplexes form antiformal stacks while others form independently spaced ramp anticlines (compare Fig. 1e and i)?
5. Is there any relation between the variations in duplex geometries and the relative mechanical properties of the décollements and intervening rocks?
6. What controls the timing of structures within a thrust belt?

To investigate these questions, we chose a physical modeling approach similar to Willis' (1892). This method has certain advantages over analytical modeling. Like analytical models, each parameter, such as stratigraphic geometry, décollement strength or shortening rates, can be varied in isolation. Unlike analytical models, faults form spontaneously in the model without predetermining their location and spacing, and physical models can easily handle large finite strains. Physical models are, however, limited by the availability of materials whose properties are reasonably scaled with respect to those of their natural, geologic analogs (e.g. their ability to deform under the effect of gravity), and therefore require more drastic initial simplifications.

The purpose of this paper is to use physical models to systematically examine the effects of (1) deformation rate, (2) décollement strength, and (3) décollement stratigraphic pinchouts on the style of thrust belts and duplexes. We focused on the development of passive- versus active-roof duplexes (Fig. 2), and the prediction of what types of styles and structures one might expect to find together (e.g. does underthrusting occur with imbricate stacks, large flat-on-flat thrust sheets, both, etc?). A knowledge of what styles one might find together has potential to provide a tool to help determine the sub-surface style of a duplex based on more limited data such as surface geology alone.

Our physical models were made of dry quartz sand and two types of silicone polymers. The deformation of quartz sand obeys a Mohr–Coulomb criterion of failure with negligible cohesion and an angle of internal friction close to 30°. Because of this property, the sand is used as an analog for brittle sedimentary rocks. In the models, the sand layers are of various colors, but have identical mechanical properties. We used two linear viscous silicone polymers

Table 1
Summary of model duplex conditions and observations

Model number	327	330	339	323, 354, 355	328	343	342	309	310
Shortening rate and description	5 mm/h	10 mm/h	50 mm/h	100 mm/h	500 mm/h	100 mm/h basal PDMS	100 mm/h roof PDMS	5 mm/h roof pinch-out	10 mm/h roof pinch-out
Prototype viscosity[a]	10^{17} Pa s	5×10^{17} Pa s	10^{18} Pa s	5×10^{18} Pa s	10^{19} Pa s	floor: $\approx 10^{19}$; roof: 5×10^{18} Pa s	flr: 5×10^{18}; roof: $\approx 10^{19}$ Pa s	10^{17} Pa s	5×10^{17} Pa s
Percent total shortening	36%	27%	26%	26%	33%	26%	26%	14%	27%
Extent of roof décollement	Ends 8 cm from left	Continuous	Continuous	323 ends 10 cm from left	Continuous	Continuous	Continuous	Ends 46 cm from left	Ends 45 cm from right
Thrust sheet length[b]	7.4–37.0 (21.8)	5.4–22.0 (10.0)	5.9–10.4 (7.8)	6.5–9.9 (8.6)	n/a	7.6–9.4 (8.6)	n/a	12.5–43.3 (25.0)	n/a
Thrust displacement[b]	2.6–8.3 (4.7)	1.7–5.1 (3.1)	1.2–1.7 (1.5)	0.6–1.7 (1.2)	n/a	0.4–2.5 (1.7)	n/a	2.5–3.8 (3.2)	n/a
Deformation of thrust blocks	Very little	Very little	Box folding, thickening	Box folding, thickening	Box folds cut by later thrusts	Little. minor box folding	n/a	Very little	n/a
Duplex geometry		Antiformal stack	Spaced ramp a/c	Spaced ramp a/c to isoclinal folds	Fold dominated	Spaced ramp a/c	Fold dominated	Spaced ramp a/c	Folded thrusts
Vergence within duplex	Both directions	Forward, one backwards thrust sheet	Generally forward	Generally forward	Forward on late thrusts (otherwise symmetrical)	Forward	Forward to symmetrical	Both directions	Both directions
Lateral continuity of duplex	Continuous across model width	Continuous across model width	Structures overlap and transfer displacement	Structures overlap and transfer displacement	Structures overlap and transfer displacement	Continuous with some displacement transfer	Folds locally develop into thrusts	Structures continuous, but change vergence	Structures continuous, but change vergence
Cover response	Active-roof (decoupling)	Active-roof (decoupling)	Passive-roof (coupling; local underthrust)	Passive-roof (coupling; local underthrust)	Harmonically folds (strong coupling)	Passive- to active-roof transitional	Harmonically folds (strong coupling)	Underthrust, but decoupling	Decoupling
Structural relief of duplex	High (2–3 times layer thickness)	High (2–3 times layer thickness)	Low (1.5–2 times layer thickness)	Low (1.5–2 times layer thickness)	Low (1.5–2 times layer thickness)	Medium (2–2.5 times layer thickness)	Low (<1.5 times layer thickness)	Medium (2 times layer thickness)	Medium (2 times layer thickness)
Structural evolution	Coevally	Coevally	Sequentially forward	Sequentially forward	Sequentially forward	Sequentially forward	Sequentially forward	Coevally	Coevally
Overall sand-silicone wedge shape	Gentle taper <2°	Gentle taper ≈2°	Gentle taper on top, steep front (6–10°)	Gentle taper on top, steep front (8–12°)	Steep taper 12–14°	Steep taper 10–12°	Medium taper 6–10°, gentle taper on top	Very gentle	Very gentle
LPS	8–9% mainly early	8–10% mainly early	9–11% mainly late	10–12% mainly late	10–14% mainly late	8–10% mainly late	10–14% mainly late	<8% early	8–10% mainly early

[a] Assumes endwall displacment rate is the equivalent of 10 cm/year.
[b] Normalized to a sand thickness of 1 cm for comparison. All lengths are in centimeters, average in parentheses.

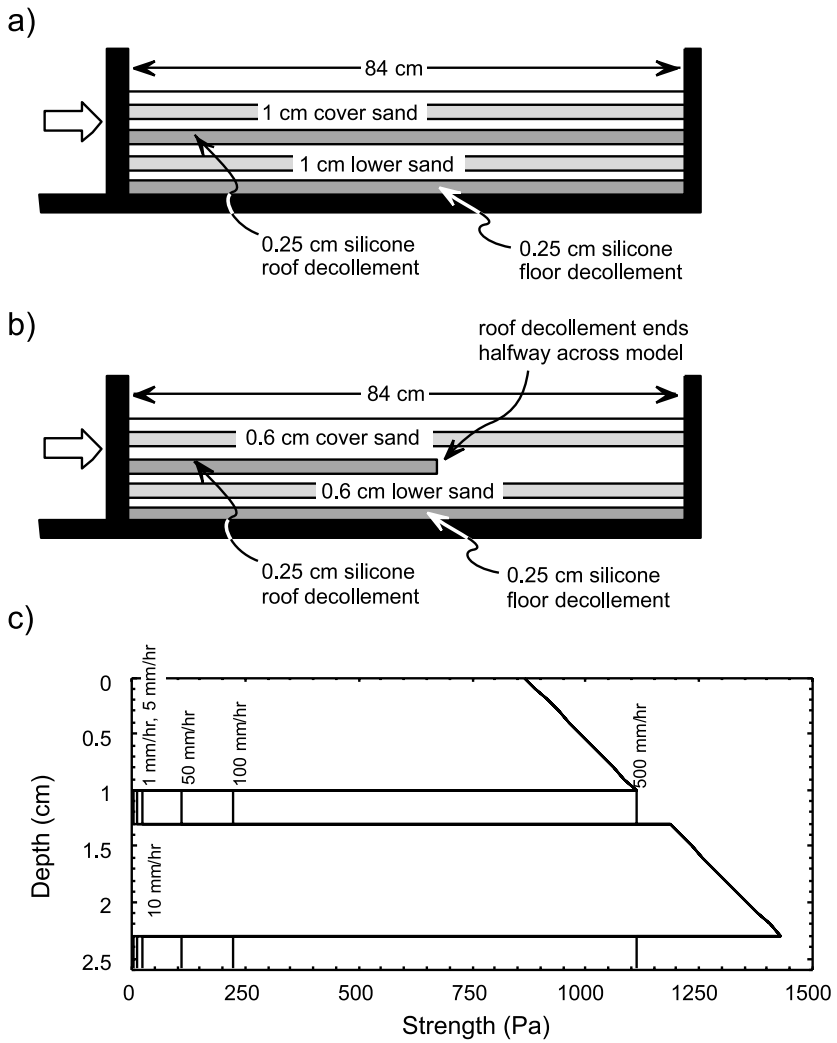

Fig. 3. (a) Schematic cross-section of the model setup for a double décollement stratigraphy. The left wall is the pushing wall and the right wall remains stationary. (b) Schematic cross-section of the model setup for a double décollement stratigraphy with a pinch-out. Layers that pinch-out can extend from the left side to the center of the model (#310) or from the center to the right side of the model (#309). (c) Strength profiles for the two décollement models as they vary with shortening rate.

as analogs of weak décollement layers, such as evaporites or overpressured shale: RG20, manufactured by Rhône-Poulenc, US, is a transparent silicone polymer having a viscosity of 1×10^4 Pa s; Silbione Silicone, a pink, dilatant compound manufactured by Rhône-Poulenc, France, has a viscosity of 2×10^4 Pa s. Silbione Silicone therefore simulated a stronger décollement. The scaling relationships between the models and nature are described in Appendix A.

2. Model setup

We ran 11 experiments (Table 1) designed to investigate various parameters such as décollement strength and initial stratigraphic geometry. The models were initially 41 cm wide and 86 cm long. The stratigraphy for nine of the 11 models is illustrated in Fig. 3a and Table 1 and consisted of the following (from bottom to top):

- a 2.5-mm-thick basal layer of viscous silicone, representing the floor décollement.
- a 10-mm-thick brittle layer made of five 2-mm-thick layers of sand of various colors but identical physical properties, which we will refer to as the lower sand sequence.
- an upper 2.5-mm-thick layer of viscous silicone, representing the roof décollement.
- a 10-mm-thick upper sand layer comprising five 2-mm-thick layers of sand of various colors, which we will refer to as the cover sand sequence.

For two of the 11 models, the two sand units were 6 mm thick (each one comprising three 2-mm-thick sand layers), and the upper silicone layer extended only halfway across

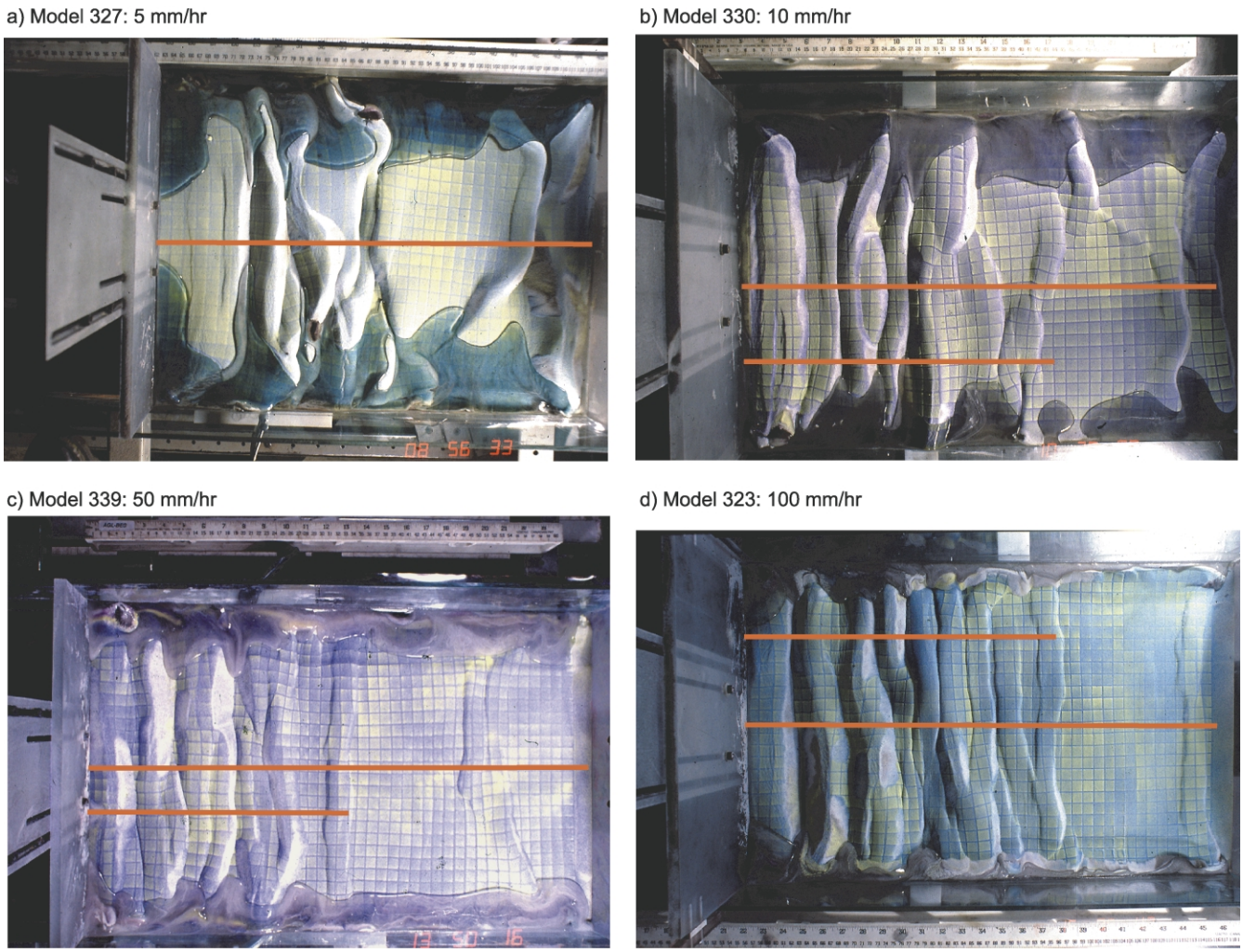

Fig. 4. Overhead photographs of models with two silicone décollements. Solid lines indicate cross-section locations for Figs. 5 and 6. The maps are lit from the right side (foreland), so slopes dipping to the right appear bright and those dipping to the left appear dark. The pushing wall for the model is on the left-hand side as it is in all cross-sections. (a) Model 327: 5 mm/h, (b) Model 330: 10 mm/h, (c) Model 339: 50 mm/h, (d) Model 323: 100 mm/h.

the length of the model to simulate a stratigraphic pinch-out of the roof décollement (Fig. 3b).

The model materials were chosen to represent rocks of the upper crust. Depending on the scaling ratios, the thickness of models represents 2.5 to 5 km of stratigraphy. The sand layers scale to brittle sedimentary rocks such as clastics or carbonates, which obey a Mohr–Coulomb failure criterion. The silicone scales to viscous evaporites such as rocksalt and gypsum. It can also be scaled to represent overpressured mudstones as a frictional plastic material. In general, silicone in models deformed at shortening rates of 1–10 mm/h corresponds to either a salt décollement, or a highly overpressured mudstone décollement (fluid pressure that exceeds 90% of the overburdern pressure), whereas silicone shortened at 50–500 mm/h represents a shale décollement with moderate to no overpressure. For more details, please see Appendix A.

Our models were designed to examine several effects. (1) We varied the shortening rate, which controls the strength of the décollements (Fig. 3c), from 5 to 500 mm/h in five models. (2) In two experiments, we tested the effect of having different strengths for the roof and floor décollements using two different silicones, RG20 and Silbione Silicone. Under the same strain rate, Silibone Silicone modeled a stronger décollement. (3) We investigated the effects of a pinch-out of the roof décollement in two models. (4) Finally, we tested model reproducibility by running two more duplicate experiments (Table 1).

3. Effect of shortening rate on deformation style

First, we describe a series of five models that all used transparent, low-viscosity RG20 silicone as an analog for décollements. Models 327, 330, 339, 323, and 328 were shortened at rates of 5, 10, 50, 100, and 500 mm/h, respectively (Table 1). Overhead (map) photographs of the surface deformation for the first four models are shown in Fig. 4a–d. For the two models deformed slowly (Models 327 and 330), duplexes that consisted of large displacement

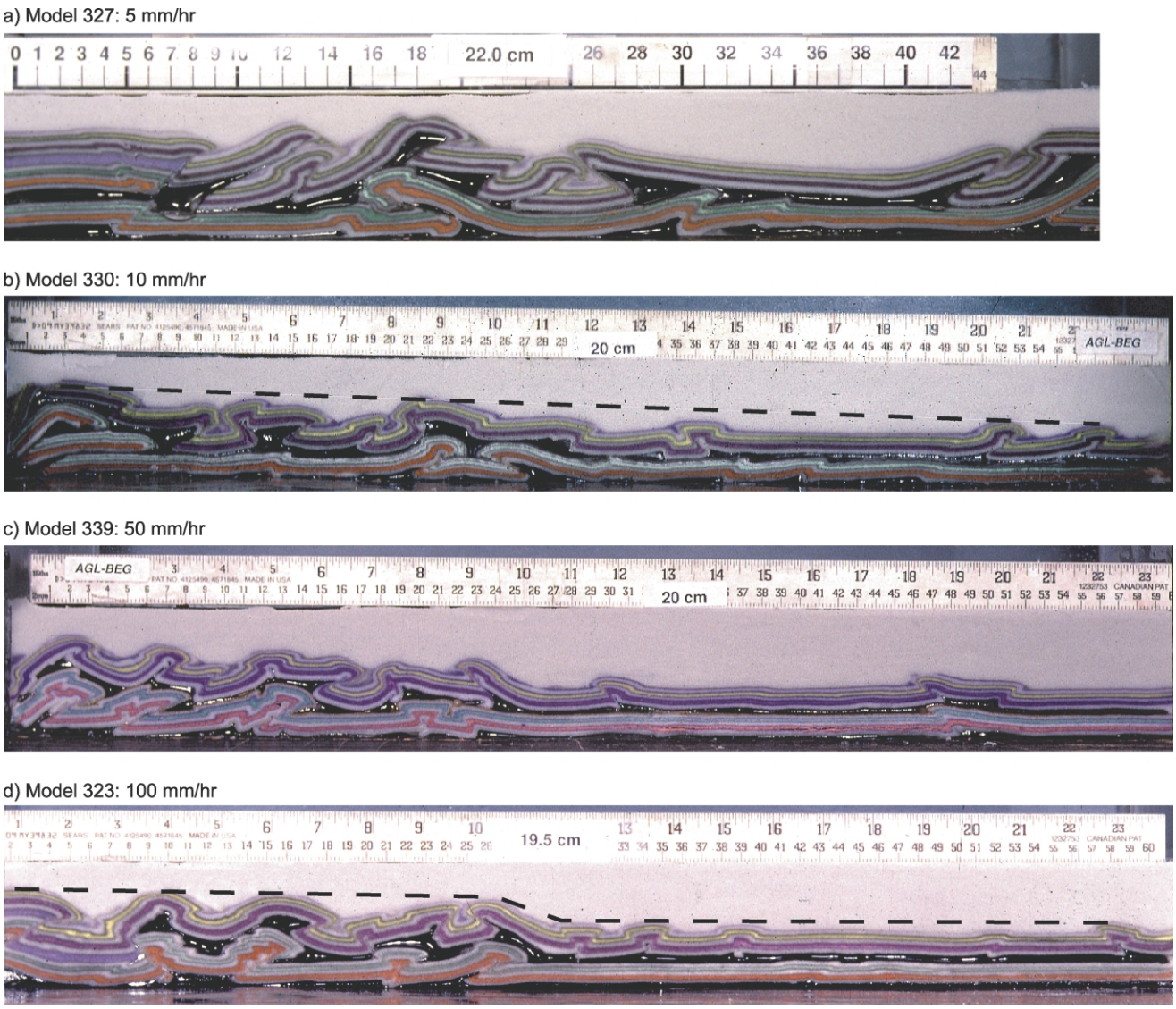

Fig. 5. Full-length cross-sections of four double décollement models. Each model is located 20 cm from the model sidewall (see locations on Fig. 4). Displacement rates vary as follows. (a) Model 327: 5 mm/h, (b) Model 330: 10 mm/h, (c) Model 339: 50 mm/h, and (d) Model 323: 100 mm/h. The silicone appears as a glossy black layer. Sand layers have different colors, but have identical mechanical properties. The thick, uppermost white sand layer was added after deformation to preserve the model topography. Dashed lines show taper profiles referred to in the text.

horse blocks formed antiformal stacks or large repetitions of section (Figs. 5a and b and 6a). In the lower sand sequence of Model 330, in front of the antiformal stack, another structural high consisting of both a backthrust and forethrust formed. The horses and thrusts forming the structural highs in the lower sand were continuous along strike across the entire width of the model (Fig. 7a). Above the structural highs in the lower sand, the cover sand remained undeformed or was slightly stretched. Extension was accommodated by a small graben above the antiformal stacks (Fig. 6a). In between and in front of the structural highs, the cover sand was structurally repeated on thrust faults (Figs. 5b and 6a).

When we subjected similar models to higher shortening rates (Models 339 and 323), the structural wedge taper of the lower sand sequence decreased, while the overall wedge taper of the whole model increased. The displacement on individual horses in the lower sand decreased. In addition, the horse blocks thickened by box folding and minor backthrusting (Figs. 5c and d and 6b and c). Because their displacement was low, the horses were not stacked as before, but formed closely spaced, individual anticlines. Fewer horses verged backwards. The thrusts that subtend the horse blocks were less continuous along strike and tended to overlap in transfer zones (compare Fig. 7a with Fig. 7b and c). Also at higher shortening rates, only minor faulting deformed the cover sand sequence. Above individual horse blocks, shortening was accommodated mainly by folding. A small backthrust occasionally formed above the frontal portion of a horse block, and a forethrust often formed there as well (Fig. 5c and d).

a) Model 330: 10 mm/hr

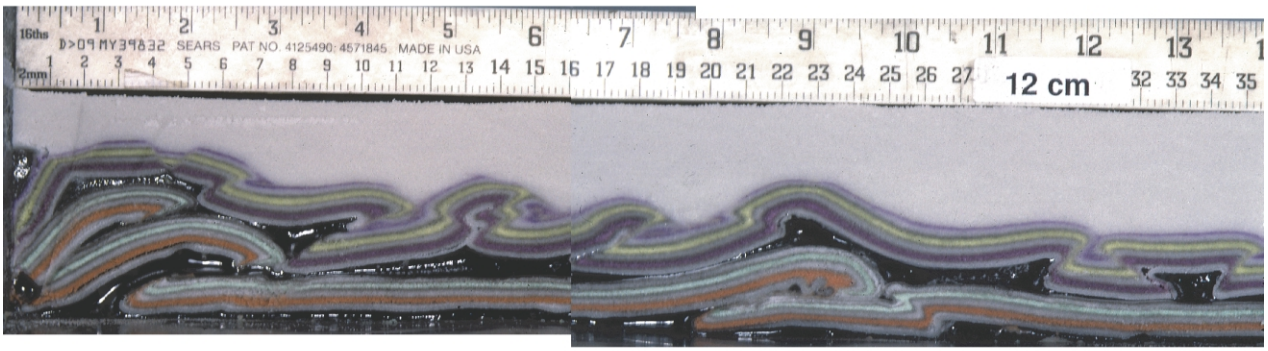

b) Model 339: 50 mm/hr

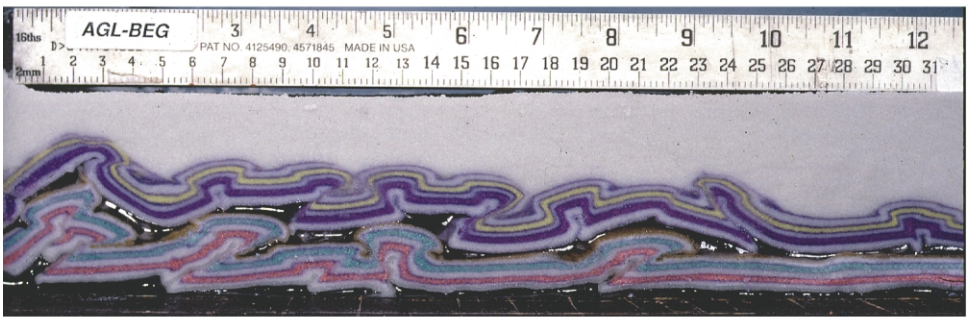

c) Model 323: 100 mm/hr

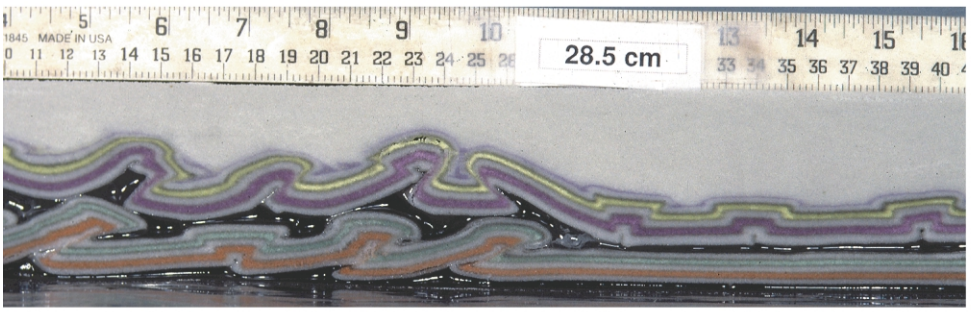

d) Model 328: 500 mm/hr

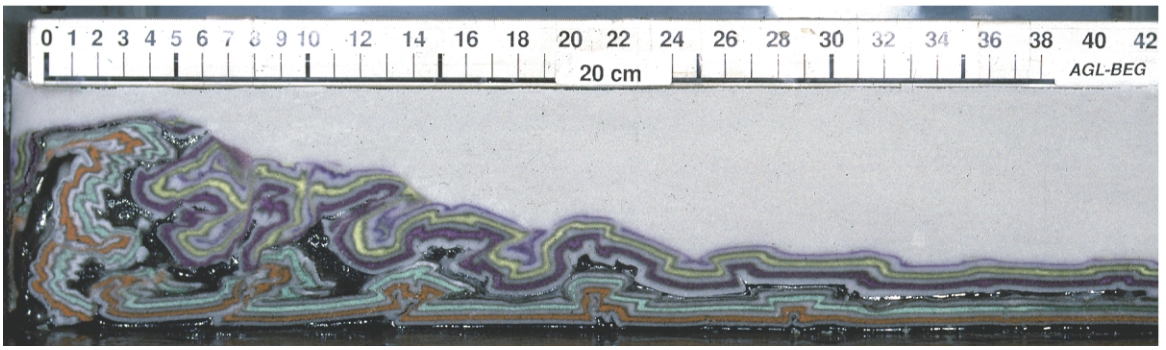

Fig. 6. Close-up cross-sections of four double-décollement models. The locations of the first three sections are shown in Fig. 4. (a) Model 330: 10 mm/h, section is 12 cm from the model sidewall. (b) Model 339: 50 mm/h, section is 16 cm from the model sidewall. (c) Model 323: 100 mm/h, section is 28 cm from the model sidewall. (d) Model 328: 500 mm/h, section is 20 cm from model sidewall.

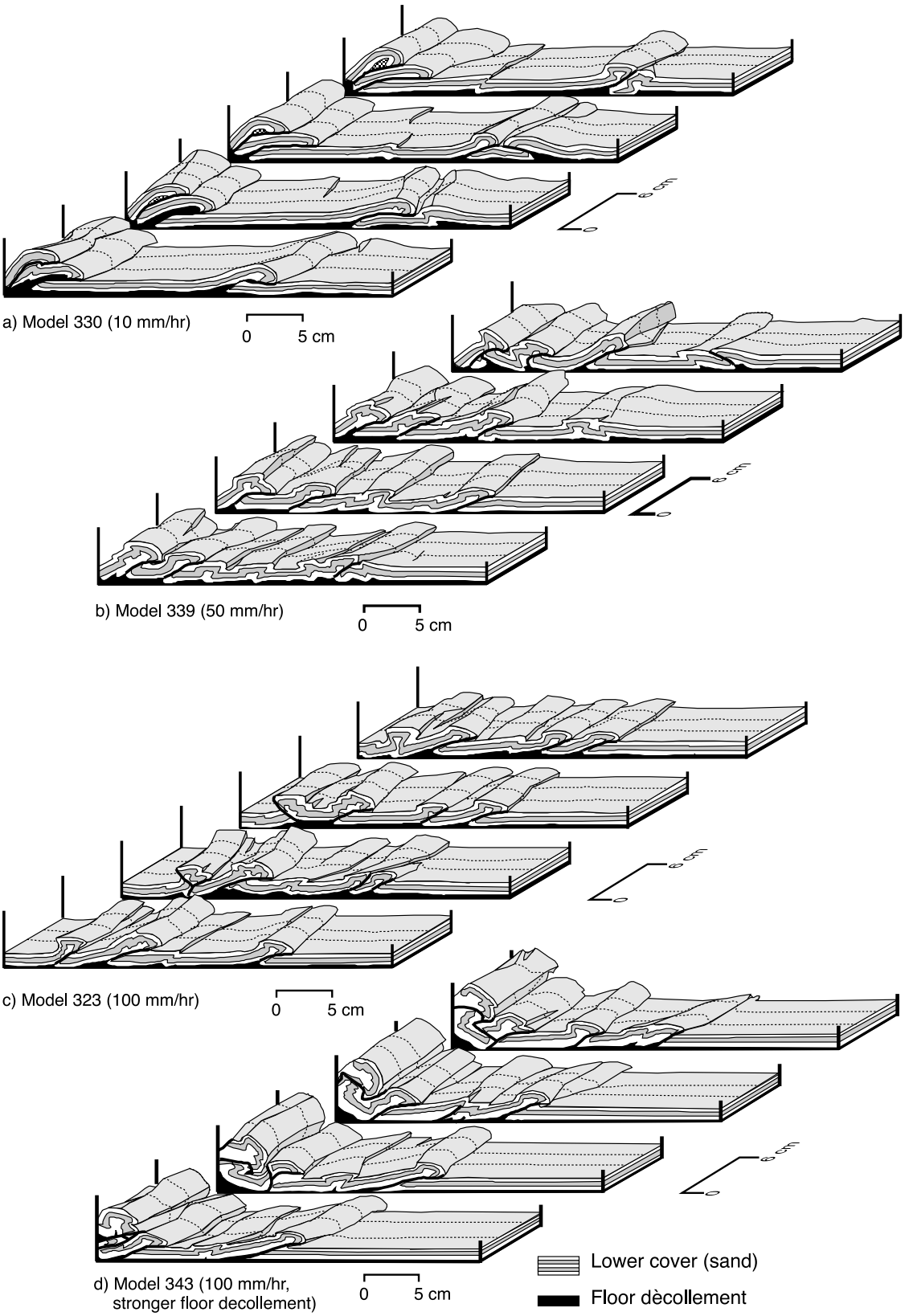

Fig. 7. Perspective views illustrate horse-block geometries in four different models. The complete sections for the 20 cm cut are shown in Fig. 5 for Models 330, 339, and 323. (a) Model 330: 10 mm/h. (b) Model 339: 50 mm/h. (c) Model 323: 100 mm/h. (d) Model 343: 100 mm/h with Silibone Silicone as a basal décollement in place of RG20. Sections from this model are shown in Fig. 9.

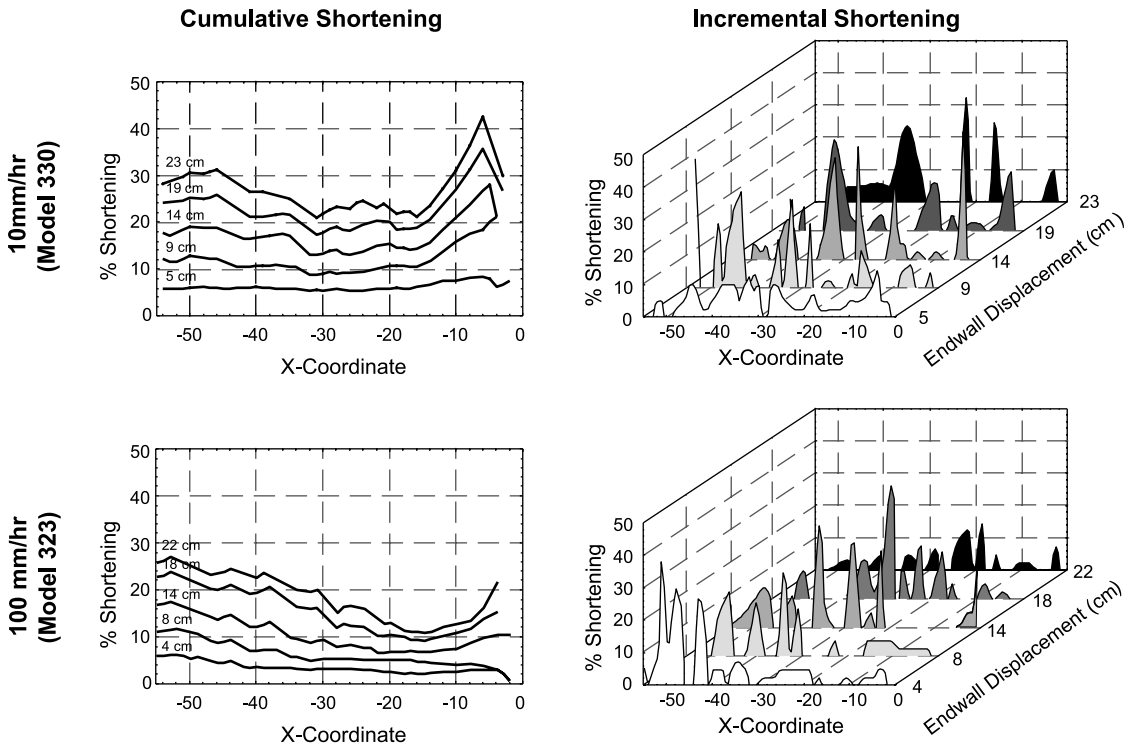

Fig. 8. Deformation-history graphs for two double-décollement models (measured from overhead photographs). The left column of graphs shows the total amount of shortening in each model at five different values of displacement of the moving wall. The right column of three-dimensional graphs shows the portion of the model that shortens between each of the five time increments. A spike indicates that a structure that localizes shortening (e.g. a fault or kink fold) is active during that time increment. A broad area of low shortening indicates bulk shortening of the sand layer in that region during that time increment. (a) Model 330: 10 mm/h. (b) Model 323: 100 mm/h.

4. Effect of shortening rate on structural evolution

The evolution of the models varied with the imposed displacement rate. In slowly shortened models, a gentle topographic taper of about 1–2° during the early stages of deformation and was maintained throughout the deformation history. In order to maintain the same taper, the deeper structures needed to continuously accumulate strain throughout the deformation history, and several out-of-sequence thrusts form within the cover (Fig. 8a). In contrast, a high frontal taper of 10° or more formed in models subjected to rapid shortening. This region of high taper developed while a horse block in the lower sand sequence moved up a ramp. Once the frontal taper reached about 10°, the horse block stopped growing and a new one formed in front of it (Fig. 8b). Thus, the horses in the fast models propagated sequentially from the hinterland to the foreland. Once a new frontal structure had formed, little deformation took place in the abandoned structure (Fig. 8b). This produced a low-taper region located behind a steep-taper front. Although the material in the region of low taper kept moving forward during subsequent shortening, it was not significantly internally deformed.

Model 328, shortened at the highest rate (500 mm/h), shows yet another scenario (Fig. 6d). The finite amount of shortening for this model was 33%, higher than the 26% finite shortening in the previous models. Because of the high imposed displacement rate, the upper silicone layer was comparatively very strong, which allowed a strong coupling between the overlying and underlying sand layers. The main structures, however, were neither horse blocks nor thrust faults, but rather symmetrical box folds. With further shortening, the folds were then cut by thrusts faults, forming complicated structures at the back end of the model. As in the other two fast-shortening models, structures propagated sequentially forward. But the early folds were subsequently modified by late deformation.

5. Effect of different décollements on style

In the previous series of models, both décollements were made of the same kind of silicone (RG20) and hence had similar rheological properties. In the next set of models we tested the effect of a having a stronger roof or floor décollement by using the more viscous Silbione Silicone. All the models in this series were shortened at a rate of 100 mm/h (Table 1).

Model 343 was constructed with a more viscous basal décollement. The style of deformation did not differ much from Model 323, which has two RG20 silicone décollements, (Figs. 6c and 9a). Overall, the deforming wedge developed a higher relief, as would be expected with a stronger décollement. The increase in relief was achieved by

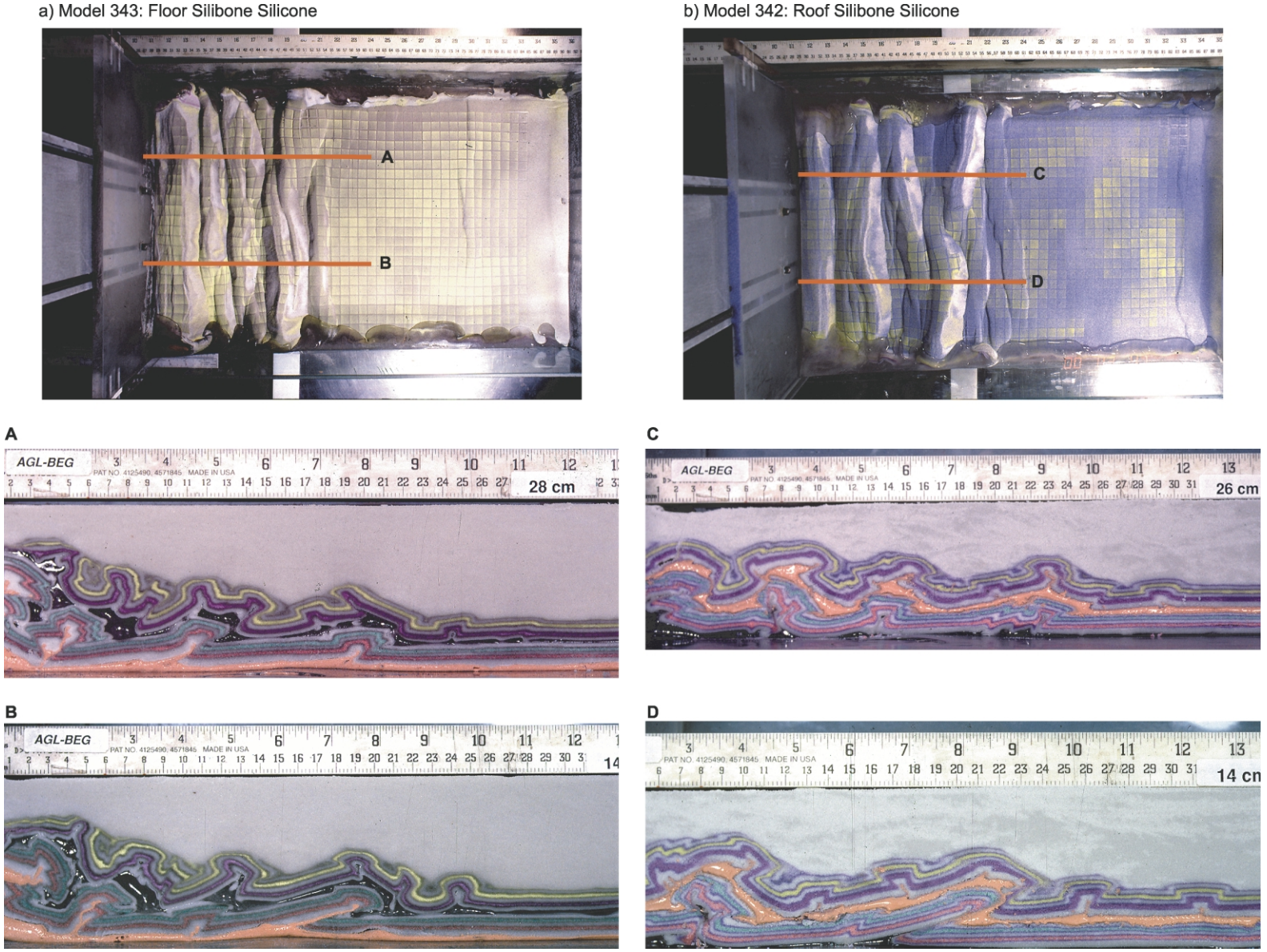

Fig. 9. Overhead photographs and cross-sections of two models with both RG20 and Silibone Silicone décollements. The Silibone Silicone is two to three times more viscous than the RG20 silicone and it shows in the photographs as a shiny pink layer. Both models were shortened at 100 mm/h. (a) The left column shows photos from Model 343, which has a floor décollement of Silibone Silicone. The sections, denoted with capital letters A and B, are located 28 and 14 cm from the model sidewall. (b) The right column shows photos from Model 342, which has a roof décollement of Silibone Silicone. The sections, denoted with capital letters C and D, are located 26 and 14 cm from the model sidewall.

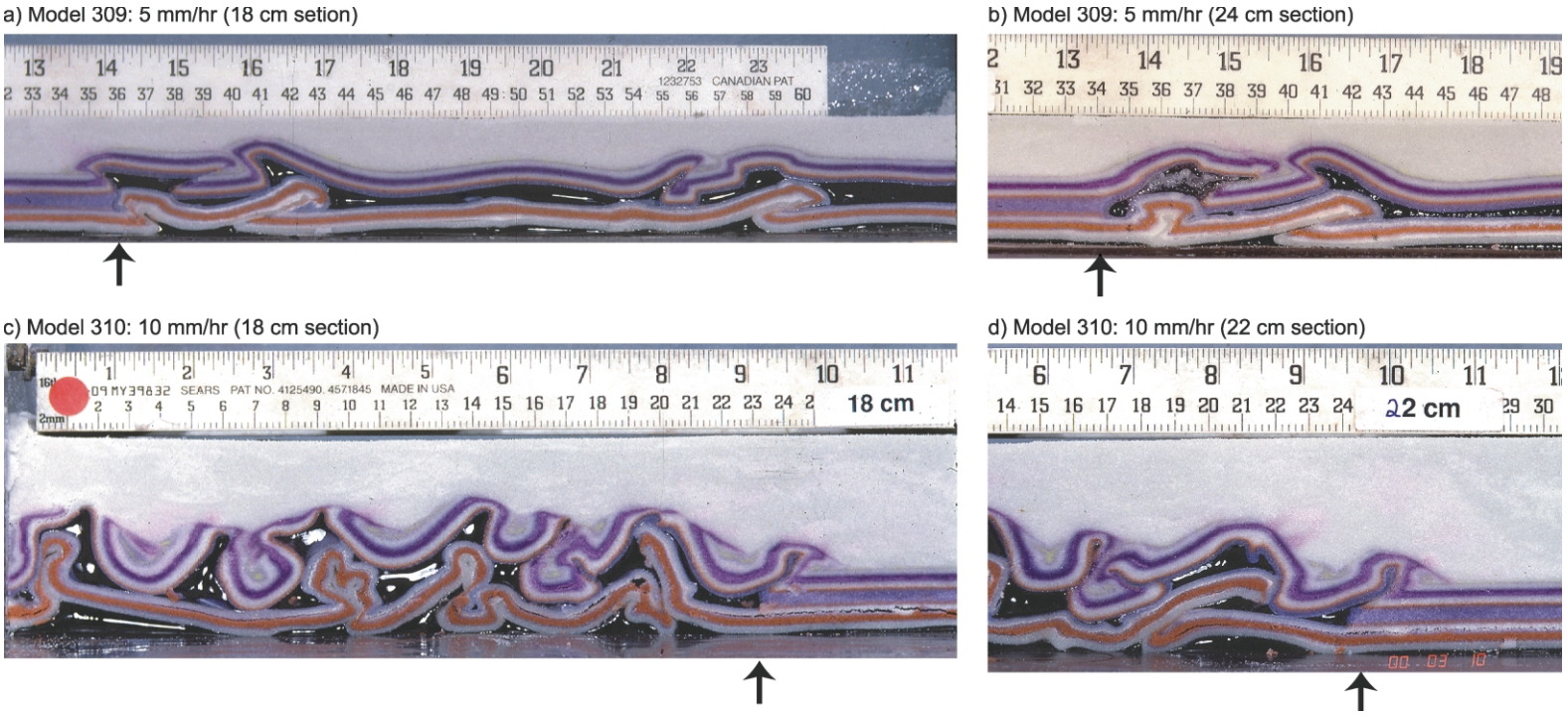

Fig. 10. Cross-sections of Models 309 and 310 having pinch-outs of the roof décollement. Model 309 was shortened at 5 mm/h and Model 310 at 10 mm/h. Displacement of the moving wall in Model 310 is about twice that of Model 309 (Table 1). (a) Model 309, cross-section of entire roof décollement 18 cm from the model sidewall. (b) Model 309, close-up of the pinch-out in a section 24 cm from the model sidewall. (c) Model 310, cross-section of the entire roof décollement 18 cm from the model sidewall. (d) Model 310, close-up of the pinch-out in a section 22 cm from the model sidewall. Arrows beneath each photo show the pinch-out location.

having more displacement of the individual horse blocks within the duplex (Fig. 7d). Because of the large amounts of translation of the horse blocks, the cover could not simply accommodate all of the shortening by folding and minor faulting above the horses only, and additional structures needed to form in front of the horse blocks (Fig. 9a).

Model 342 comprised a stronger roof décollement. The deformation style tends towards folding instead of horse block formation (Fig. 9b). In general, deformation is more harmonic between the sand layers in this model. Along strike, one fold became a major thrust fault, cutting through the roof décollement (Fig. 9b).

It is interesting to note that models having similar roof-décollement strengths had similar deformation patterns, even if they had different strengths for the floor décollement. This suggests that the roof décollement properties are most important in determining the structural style.

6. Influence of décollement pinch-outs

In two models (Models 309 and 310), the roof décollement pinched out halfway across the model (Fig. 3b). The models were shortened at 5 and 10 mm/h, respectively (Table 1). The roof décollement in Model 309 pinched out to the left (away from the backstop), whereas the roof décollement in Model 310 pinched out to the right (toward the backstop). In both cases, deformation was concentrated in the part of the model where the roof décollement was present (Fig. 10). Model 309, shortened at 5 mm/h, was subjected to only 14% total shortening. However, because deformation affected only the area where the roof décollement was present, the deformed portion actually recorded 26% of shortening. Model 310 was shortened at 10 mm/h, up to 27% total shortening, an amount similar to that in most previous models (Table 1). Again, because deformation was concentrated in the area where the roof décollement was present, the deformed portion recorded a 56% shortening.

The latter models shared five characteristics with other models deformed slowly (e.g. Models 327 and 330): (1) long thrust sheets, (2) little internal strain within thrust sheets, (3) vergence in both directions, (4) low overall relief of the wedge, and (5) coeval growth of structures (Fig. 10). There was one significant difference between the models with and without a roof-décollement pinch-out. The thick sand layer where the roof décollement is absent, acted as a strong, rigid beam, allowing little or no deformation to occur there. This caused underthrusting of the cover sand sequence by horse blocks in the lower sand sequence, creating a passive-roof geometry even though the roof décollement decoupled the upper and lower brittle sand layers. However, unlike in most passive-roof duplexes, a structure consistently broke through to the surface at the location of the décollement pinch-out.

Model 310 (Fig. 10), which was subjected to more shortening, had a complicated deformation pattern that differed from that of Model 309, which has less displacement. Model 310 was similar to Model 330, its counterpart without a pinch-out, in that the structural relief at the top of the lower sand sequence was high. The upper and lower sand layers were greatly decoupled by the roof décollement, as is attested by the fact that most structures in the upper layer were located in-between the structures of the lower layer. This model deformed by much more folding than Models 330 and 309 did (Figs. 6a and 10a and b). The presence of folded thrusts suggests that folding continued until the late stages of shortening.

7. Discussion

7.1. Comparison with a simple mechanical model

Davies and Fletcher (1990) present a simplified mechanical model for the initiation of a duplex, in which a von Mises plastic layer is overlain by a viscous layer. Their model helps explain some of the differences between physical models that have strong vs. weak décollements. Results indicate that (1) duplex initiation requires that the overlying viscous layer be weaker than the plastic layer, (2) a stronger viscous layer suppresses the formation of shear bands (thrust faults) in the plastic layer and enhances folding of the interface, (3) formation of asymmetric, foreland-verging horses requires a component of layer-parallel shear stress, otherwise symmetrical pop-up structures form.

Our model setup is similar to that used by Davies and Fletcher (1990). The lower sand layer is a plastic material with a Mohr–Coulomb failure criterion, and the overlying silicone roof décollement is viscous. Unlike their model, our models included a second sand layer above the viscous layer. Nevertheless, the results can be used to explain some of our models' results that may otherwise appear confusing or counterintuitive. In particular, under low shortening rates, structures in the model duplex are more likely to be symmetrical (e.g. Model 327, Fig. 5a; Model 330, Figs. 5b and 7b). The symmetry indicates that both away from the walls and under slow shortening, layer-parallel shear stress remains low. At higher shortening rates, the symmetry decreases, although backthrusts can still be found locally in some models (e.g. Model 339, Fig. 7b; Model 355, Fig. 11c). Overall, the number of forward-verging horses increases, owing to the increase in layer-parallel shear stress and to the increase in effective décollement strength.

However, in the uppermost range of shortening rates (e.g. 500 mm/h), this trend is reversed and structures become increasingly symmetrical with increasing shortening rate. We see this in particular in the fastest model (Model 328, Fig. 6d). Davies and Fletcher's (1990) models make this observation understandable. Under very fast shortening (500 mm/h for Model 328), viscous stresses in the silicone

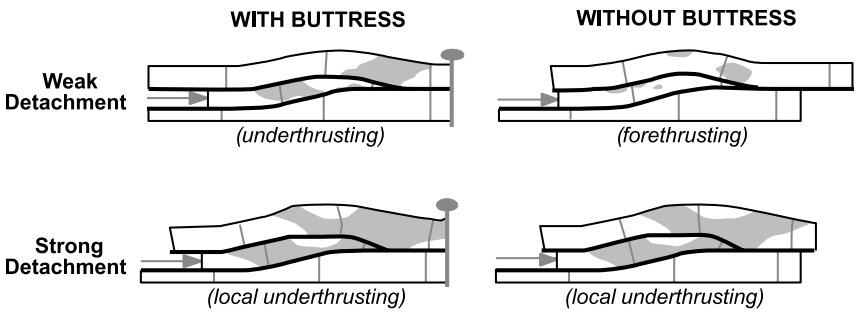

Fig. 11. Cartoons illustrating the different horse-block cover responses depending on boundary conditions and detachment strengths. The cartoons are based on results of published finite element models (Erickson, 1995; Jamison, 1996) and our physical models (see text for details).

layer become effectively greater than the strength of the sand layer (Fig. 3c). As a result, similar to Davies and Fletcher's (1990) model, thrust formation in the sand layer is suppressed and folding of the interface between the sand and silicone is enhanced. Model 328 (Fig. 6d) first deformed by folding the silicone and sand layers, as indicated by the last structure to form on the right side of the model in Fig. 6d. The folds are then later modified by thrust faulting as they become incorporated into the deforming wedge (see structures further to the left on Fig. 6d).

The concept that a strong, viscous roof décollement causes folding, rather than duplex formation, also explains why Model 342, which has a Silbione Silicone roof décollement, deforms by folding (Fig. 9). The Silbione Silicone is about two to three times as viscous as the RG20 silicone used in most of the models. Therefore, at a given shortening rate, the stresses in that silicone are two to three times greater than those in a RG20 silicone layer. Because Model 342 is deformed slowly but comprises a more viscous décollement, stresses in the silicone also approach the strength of the sand (Fig. 3c), inhibiting thrust fault formation and promoting folding of the sand-silicone interface in a manner similar to that of faster models (e.g. Model 328).

7.2. Comparison to kinematic model for duplexes

Boyer and Elliott (1982) propose relationships between fault spacing and displacement. In nature, duplex style ranges from antiformal stacks accommodating large displacements to individually spaced ramp anticlines accommodating smaller displacements (e.g. Fig. 1e vs. Fig. 1i). Boyer (1992) suggests that the structural style might vary as a duplex grows by simultaneous slip on fault planes within a duplex. Early stages, when fault displacements are small, are characterized by spaced-ramp anticlines. Later, as fault displacements increase, the duplex grows to resemble the idealized flat-top duplex model, and it finally becomes an antiformal stack.

Our models show a similar variation in geometry as a function of shortening rate or décollement strength. Antiformal stacks form in models deformed slowly or having weak décollements, whereas spaced-ramp anticlines form in models deformed rapidly or having strong décollements (Fig. 6). Our model results suggest that the variation in geometry is not solely controlled by the amount of coeval slip along multiple fault planes. Instead, the amount of slip, and the resultant geometry is a function of (1) the décollement's strength and (2) the coupling between the horse blocks and the cover. For the slow models, the silicone is weak enough to allow for large displacements on thrusts. As a result, the horses and cover are decoupled. Structures in the cover develop far from the culminations in the lower sand layer. In contrast, the silicone acts stronger in the fast models. It thickens in front of and above the horse blocks, resisting their motion. As a result, the horses thicken internally, often by box folding. Structures in the cover form directly above the horse blocks.

7.3. Triangle zone and passive-roof duplex formation

Several recent studies have examined triangle zone mechanics. Jamison (1993) uses the critical-wedge theory (Dahlen et al., 1984) to investigate how much a preexisting backthrust can slip. Erickson (1995) investigates triangle zones using finite-element models. His models require a foreland 'buttress' or pinline, beyond which the cover sequence cannot slide. His results are that more underthrusting occurs where friction along the roof detachment is low or where the cover is strong. In the absence of any pinline very little underthrusting takes place (Erickson, 1995). A similar study by Jamison (1996) on the nature and distribution of deformation in a preexisting triangle zone also predicts that (1) more underthrusting occurs where friction along the roof detachment is low or where the cover is strong and (2) higher shear resistance leads to horse-block thickening, rather than underthrusting the cover. Both studies (1) assume preexisting fault planes, (2) examine the growth of triangle zones by slip along those preexisting faults, and (3) include the foreland pinline as a required boundary condition.

The boundary condition of a foreland pin line would seem to apply to our models as well. No deformation can occur beyond the endwall of the model. However, the basal viscous shear applied at the base of the brittle cover and exerted by the décollement is also resisting shortening and

forward propagation of the fold and thrust belt. Our models show a difference in style of propagation that reflects the influences of both the basal viscous shear and the buttressing effect of the model endwall. In models deformed under fast shortening rates, structures propagated forward and the cover in the distant foreland was not affected by shortening. By contrast, in models shortened under slow strain rates, structures did not propagate systematically forward. Even during early deformation, folds formed in the foreland, far from the moving wall. Younger folds formed later, near the model's center. Costa and Vendeville (2002) reported a similar mode of propagation in experiments having a single, weak, viscous décollement.

Costa and Vendeville (2002) showed that during shortening above a very weak décollement, the length of the critical wedge could exceed the length of the model box. The fold-and-thrust belt therefore does not propagate forward in a piggyback fashion. Folds and thrusts nucleate early on both sides of the box, younger structures form near the model center, and all structures continue to grow coevally. By contrast, in models having a stronger décollement (i.e. higher applied strain rate), because the length of the critical wedge is less than that of the model box, deformation of the brittle cover is resisted entirely by basal viscous shear and is therefore insensitive to the presence of the distal buttress.

Another way to illustrate this difference in structural behavior is to estimate the maximum length of a brittle layer that can be translated above a viscous décollement under the effect of a push from behind. Assuming no distal buttress, translation of a brittle slab is resisted at the base solely by viscous shear of the underlying décollement, exerting the following force:

$$F_v = \frac{v\eta l_c w}{t_d},$$

where F_v is the force resisting viscous shear, v is the shortening velocity, η is the silicone viscosity, l_c is the maximum length of the brittle slab, w is the model width, and t_d is the décollement thickness.

On the other hand, the brittle layer may fail in compression if the applied horizontal force exceeds the layer's strength, as defined below:

$$F_b = 3w\int_0^h \rho g z \mathrm{d}z = \frac{3w\rho g h^2}{2},$$

where F_b is the force to overcome the brittle sand layer strength, w is model width, r is sand density, g is acceleration due to gravity, and h is brittle layer thickness.

By setting the viscous force resisting translation of the brittle slab, F_v, equal to the force required to deform the brittle slab, F_b, the two previous equations can be combined to estimate the critical length of a brittle slab, above which the resisting, viscous basal force will exceed the brittle layer's strength:

$$l_c = \frac{3\rho g h^2 t_d}{2v\eta}.$$

Critical length represents the maximum length of the brittle slab that can be translated forward without causing compressional failure of the slab. When it is applied to our models, we can compare the calculated critical length with the length of the model's box. In cases where the critical length is lower than the model's length, forward fold-and-thrust propagation is resisted entirely by basal viscous shear, and deformation of the brittle layer is oblivious to whether a distal buttress (the end wall) is present. By contrast, in cases where the critical length exceeds the length of the model's box, the buttressing effect of the distal pin line has some control on the formation of contractional structures in the brittle layer.

Given the dimensions and rheological properties of our models (Fig. 3; Tables 2 and 3), the calculated values of critical lengths for velocities of 5, 10, 50 and 100 mm/h are 33.0, 16.5, 3.3 and 1.6 cm, respectively. This calculation suggests that only models run slower than ours will be strongly sensitive to the buttressing influence of the distal endwall. Furthermore, fold-and-thrust propagation in models that were shortened at 50 and 100 mm/h, having critical lengths much shorter than the box length, was controlled solely by basal viscous shear, rather than by the distal endwall.

The models shortened at 5 and 10 mm/h also have calculated lengths that are shorter than the model box length. Still, we observed structures forming near the endwall early in these model histories and we interpret this as an end effect. In practice, our calculations tend to underestimate the critical length of the brittle layer for two reasons. First, folds and thrusts forming near the moving wall may accommodate part of the imposed displacement. The displacement rate, and hence, the basal viscous shear force in front of these folds and thrusts, is lower, and the associated critical length greater. Second, folding and thrusting increase the overall thickness of the brittle layer, thereby increasing its strength. A longer span of the thickened, brittle layer can therefore be translated.

Following the argument above, in most of our models, the deformation of the cover is minimally affected by the model endwall as a pinline. Also, none of our models require a preexisting backthrust. As a result, our observations are, in part, opposite of those of the mechanical

Table 2
Scaling properties of dry sand

	Model scale	Natural scale	Model-to-prototype ratio
Length	1 cm	1 km	10^{-5}
Density	1.25 g cm^{-3}	2.5 g cm^{-3}	0.5
Gravity	980 cm s^{-2}	980 cm s^{-2}	1.0
Stress	250 Pa	5×10^7 Pa	5×10^{-6}

Table 3
Scaling silicone as a viscous detachment in nature

Length ratio	Silicone viscosity	Displacement rate (mm/h)	Viscosity (model)	Length ratio	Equivalent displacement in nature in equivalent of one model hour (m)	Displacement rate nature (cm/year)	Natural equivalent of one model hour (years)	Natural equivalent of one model hour (hours)	Stress ratio	Time ratio	Strain-rate ratio	Viscosity ratio	Natural viscosity (Pa s)
1 cm = 1 km	Low viscosity	1	1.00×10^{4}	1.00×10^{-5}	100	1.00	10,000	8.76×10^{7}	5.00×10^{-6}	1.14×10^{-8}	8.76×10^{7}	5.71×10^{-14}	1.75×10^{17}
1 cm = 1 km	Low viscosity	5	1.00×10^{4}	1.00×10^{-5}	500	1.00	50,000	4.38×10^{8}	5.00×10^{-6}	2.28×10^{-9}	4.38×10^{8}	1.14×10^{-14}	8.76×10^{17}
1 cm = 1 km	Low viscosity	10	1.00×10^{4}	1.00×10^{-5}	1000	1.00	100,000	8.76×10^{8}	5.00×10^{-6}	1.14×10^{-9}	8.76×10^{8}	5.71×10^{-15}	1.75×10^{18}
1 cm = 1 km	Low viscosity	50	1.00×10^{4}	1.00×10^{-5}	5000	1.00	500,000	4.38×10^{9}	5.00×10^{-6}	2.28×10^{-10}	4.38×10^{9}	1.14×10^{-15}	8.76×10^{18}
1 cm = 1 km	Low viscosity	100	1.00×10^{4}	1.00×10^{-5}	10000	1.00	1,000,000	8.76×10^{9}	5.00×10^{-6}	1.14×10^{-10}	8.76×10^{9}	5.71×10^{-16}	1.75×10^{19}
1 cm = 1 km	Low viscosity	500	1.00×10^{4}	1.00×10^{-5}	50000	1.00	5,000,000	4.38×10^{10}	5.00×10^{-6}	2.28×10^{-11}	4.38×10^{10}	1.14×10^{-16}	8.76×10^{19}
1 cm = 1 km	High viscosity	1	2.00×10^{4}	1.00×10^{-5}	100	1.00	10,000	8.76×10^{7}	5.00×10^{-6}	1.14×10^{-8}	8.76×10^{7}	5.71×10^{-14}	3.50×10^{17}
1 cm = 1 km	High viscosity	5	2.00×10^{4}	1.00×10^{-5}	500	1.00	50,000	4.38×10^{8}	5.00×10^{-6}	2.28×10^{-9}	4.38×10^{8}	1.14×10^{-14}	1.75×10^{18}
1 cm = 1 km	High viscosity	10	2.00×10^{4}	1.00×10^{-5}	1000	1.00	100,000	8.76×10^{8}	5.00×10^{-6}	1.14×10^{-9}	8.76×10^{8}	5.71×10^{-15}	3.50×10^{18}
1 cm = 1 km	High viscosity	50	2.00×10^{4}	1.00×10^{-5}	5000	1.00	500,000	4.38×10^{9}	5.00×10^{-6}	2.28×10^{-10}	4.38×10^{9}	1.14×10^{-15}	1.75×10^{19}
1 cm = 1 km	High viscosity	100	2.00×10^{4}	1.00×10^{-5}	10000	1.00	1,000,000	8.76×10^{9}	5.00×10^{-6}	1.14×10^{-10}	8.76×10^{9}	5.71×10^{-16}	3.50×10^{19}
1 cm = 1 km	High viscosity	500	2.00×10^{4}	1.00×10^{-5}	50000	1.00	5,000,000	4.38×10^{10}	5.00×10^{-6}	2.28×10^{-11}	4.38×10^{10}	1.14×10^{-16}	1.75×10^{20}
1 cm = 2 km	Low viscosity	1	1.00×10^{4}	5.00×10^{-6}	200	1.00	20,000	1.75×10^{8}	2.50×10^{-6}	5.71×10^{-9}	1.75×10^{8}	1.43×10^{-14}	7.01×10^{17}
1 cm = 2 km	Low viscosity	5	1.00×10^{4}	5.00×10^{-6}	1000	1.00	100,000	8.76×10^{8}	2.50×10^{-6}	1.14×10^{-9}	8.76×10^{8}	2.85×10^{-15}	3.50×10^{18}
1 cm = 2 km	Low viscosity	10	1.00×10^{4}	5.00×10^{-6}	2000	1.00	200,000	1.75×10^{9}	2.50×10^{-6}	5.71×10^{-10}	1.75×10^{9}	1.43×10^{-15}	7.01×10^{18}
1 cm = 2 km	Low viscosity	50	1.00×10^{4}	5.00×10^{-6}	10000	1.00	1,000,000	8.76×10^{9}	2.50×10^{-6}	1.14×10^{-10}	8.76×10^{9}	2.85×10^{-16}	3.50×10^{19}
1 cm = 2 km	Low viscosity	100	1.00×10^{4}	5.00×10^{-6}	20000	1.00	2,000,000	1.75×10^{10}	2.50×10^{-6}	5.71×10^{-11}	1.75×10^{10}	1.43×10^{-16}	7.01×10^{19}
1 cm = 2 km	Low viscosity	500	1.00×10^{4}	5.00×10^{-6}	100000	1.00	10,000,000	8.76×10^{10}	2.50×10^{-6}	1.14×10^{-11}	8.76×10^{10}	2.85×10^{-17}	3.50×10^{20}
1 cm = 2 km	High viscosity	1	2.00×10^{4}	5.00×10^{-6}	200	1.00	20,000	1.75×10^{8}	2.50×10^{-6}	5.71×10^{-9}	1.75×10^{8}	1.43×10^{-14}	1.40×10^{18}
1 cm = 2 km	High viscosity	5	2.00×10^{4}	5.00×10^{-6}	1000	1.00	100,000	8.76×10^{8}	2.50×10^{-6}	1.14×10^{-9}	8.76×10^{8}	2.85×10^{-15}	7.01×10^{18}
1 cm = 2 km	High viscosity	10	2.00×10^{4}	5.00×10^{-6}	2000	1.00	200,000	1.75×10^{9}	2.50×10^{-6}	5.71×10^{-10}	1.75×10^{9}	1.43×10^{-15}	1.40×10^{19}
1 cm = 2 km	High viscosity	50	2.00×10^{4}	5.00×10^{-6}	10000	1.00	1,000,000	8.76×10^{9}	2.50×10^{-6}	1.14×10^{-10}	8.76×10^{9}	2.85×10^{-16}	7.01×10^{19}
1 cm = 2 km	High viscosity	100	2.00×10^{4}	5.00×10^{-6}	20000	1.00	2,000,000	1.75×10^{10}	2.50×10^{-6}	5.71×10^{-11}	1.75×10^{10}	1.43×10^{-16}	1.40×10^{20}
1 cm = 2 km	High viscosity	500	2.00×10^{4}	5.00×10^{-6}	100000	1.00	10,000,000	8.76×10^{10}	2.50×10^{-6}	1.14×10^{-11}	8.76×10^{10}	2.85×10^{-17}	7.01×10^{20}

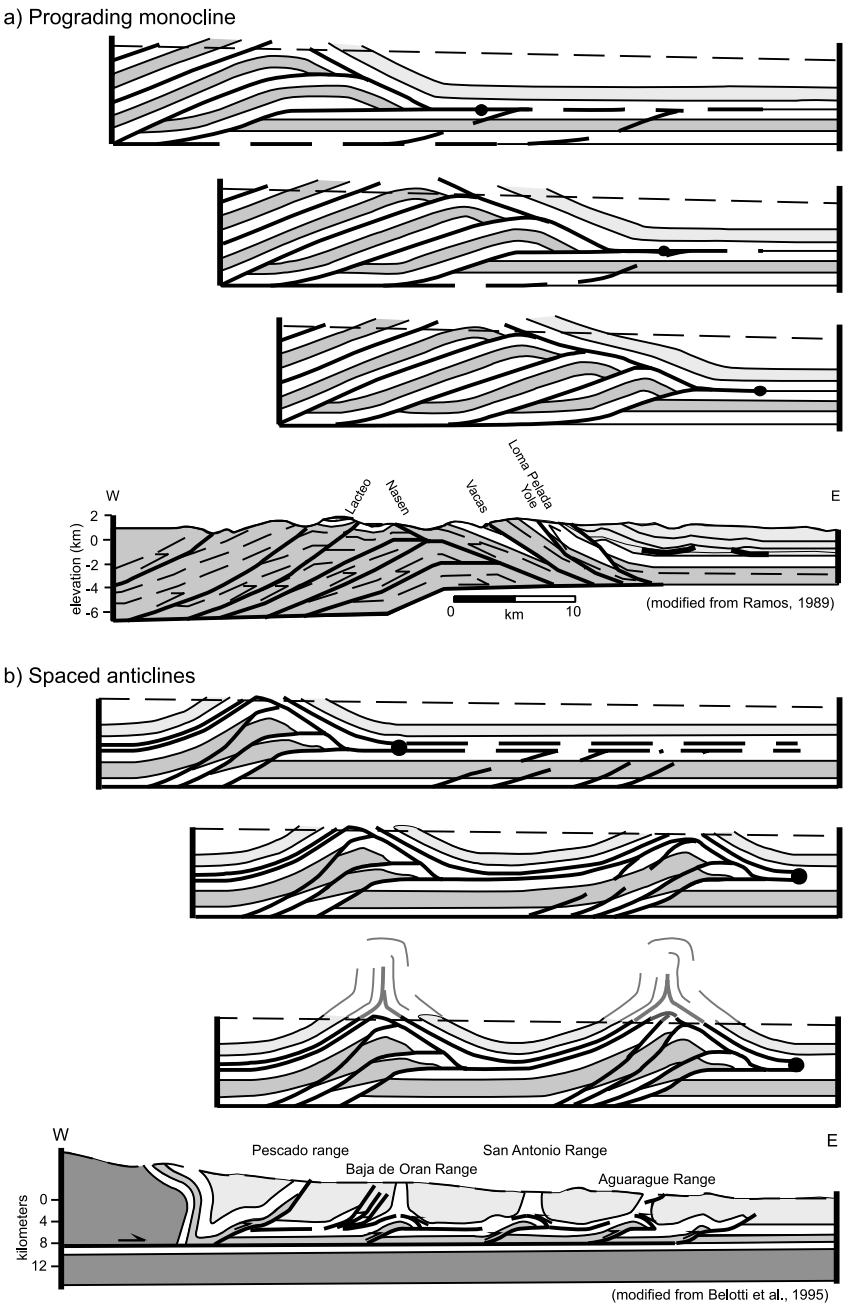

Fig. 12. Possible end-member passive-roof duplexes. (a) A prograding monocline (Jones, 1996) grows as an antiformal stack by progressively underthrusting the cover. (b) Spaced ramp anticlines locally underthrust the cover.

models described above (Erickson, 1995; Jamison, 1996). In models having a weak roof décollement, displacements are transferred by forward propagation of structures in the cover sequence (Figs. 5b and 6a), rather than by underthrusting. The forward translation of displacement is ultimately stopped by the model endwall, resulting in cover deformation at the end of the model. On the other hand, due to a higher viscous shear resistance, local underthrusting and deformation of the cover above horse blocks occurs in models having strong detachments (Figs. 5d and 6c).

The previous mechanical models predict underthrusting when our models do not because the boundary condition of the mechanical models does not allow the cover to move forward significantly, making underthrusting easier on a weaker detachment. In our models, the cover can move forward more easily on a weak décollement. Therefore, in the absence of the influence of a pinline or buttress, underthrusting can be the dominant mechanism only if the décollement is strong.

In nature, the buttress or pinline may represent the pinch-out of a stratigraphic horizon acting as roof décollement (Erickson, 1995). We have tested the influence of a pinch-out using two models (Table 1; Fig. 10). Both models are shortened relatively slowly and therefore the décollements

are weak. Without predetermined fault locations, however, the models do not develop the surficial monoclinal front characteristic of classic triangle zones. In fact, the pinch-out of the roof décollement most often localizes a thrust that breaks through the cover at the front of the deformed zone (Fig. 10). Our result is specific to the models. Natural pinch-outs are likely to be more gradual, as opposed to the blunt end of a silicone layer, and may result in a different local effect.

It is important to note that none of our models produce the large amounts of underthrusting exhibited in the finite element models (Erickson, 1995). In Erickson's (1995) model with the weakest detachment, underthrusting accommodates almost all of the motion on the horse block. Large amounts of underthrusting can also be obtained by forcefully wedging a rigid horse block beneath a strong décollement (Smart and Couzens-Schultz, 2001). This process does not require a buttress, but it does require a non-deformable horse block.

In our physical models the horse blocks could deform. Two trends observed in Jamison's (1996) finite-element models can also be found in our experiments. Stronger décollements produce more structural thickening of the horse block(s) and less forward horse-block displacement. Flat-on-flat relationships are rare when the décollements are strong, but are common in models having weak décollements (Table 1; Fig. 6a and c). Fig. 11 summarizes, in cartoon form, the results from both the mechanical models (Erickson, 1995; Jamison, 1996) and our physical models. The light gray shading highlights areas where internal strain is significant and the vertical lines highlight the relative motion of the cover and horse block.

Two end-member kinematic models have been proposed for the development of passive-roof duplexes (i.e. triangle zones). These are the prograding monocline (Fig. 12a; Jones, 1996) and the spaced-ramp anticline model (Fig. 12b; Couzens-Schultz, 1997). A prograding monocline forms as an antiformal stack that completely delaminates the cover from the underlying horse blocks, thus requiring large amounts of underthrusting at a regional scale. By contrast, in the spaced-anticline model underthrusting occurs only locally, above each horse block. Our physical models demonstrate that a passive-roof duplex with spaced anticlines forms in response to a strong décollement or to rapid shortening. None of our models produces a prograding monocline (Jones, 1996). Erickson (1995) can produce the style of underthrusting needed for such a structure with a weak detachment and a foreland buttress (Fig. 11) could cause such a buttress in nature. We modeled this situation assuming that the buttress was a stratigraphic pinch-out (Fig. 10) and found that backthrusting can occur along a weak décollement because of the presence of the pinch-out. However, the pinch-out also causes thrusts to locally form in the cover, disrupting any potential monocline. Moreover, a prograding monocline would require that the pinline moves forward during deformation, whereas a stratigraphic pinch-out remains fixed.

What is the feature missing in all the models that can produce a prograding monocline style triangle zone? One likely candidate is erosion. Mugnier et al. (1997) demonstrated that erosion of a thrust wedge enhances underthrusting. Combined erosion and deposition of synorogenic sediments decrease the overall taper of the thrust wedge. As a result, deformation would remain restricted in the area behind the thrust front, which would not propagate forward even on a weak décollement.

8. Conclusions

We started this research by asking several questions about the formation of duplexes in thrust belts. Answers to several of the questions relate to one key parameter, the strength of the décollements relative to that of the intervening and overlying rock layers. First, what are the parameters controlling the response of the cover rocks to the development of an underlying duplex? Under low shortening rates, the cover is effectively decoupled from the underlying horses, and the cover deforms in front of horse blocks, forming an active-roof duplex. Under high shortening rates, which results in a much stronger coupling, the cover is underthrusted by horse blocks forming a passive-roof duplex. The geometry of the roof décollement also affects the cover's response. If the roof décollement pinches out deformation is more dominated by underthrusting of horse blocks near the pinch-out, even if shortening is slow. However, unlike in most triangle zones, a stratigraphic pinch-out also localizes thrust faults in the cover. Finally, underthrusting on a regional scale does not occur in any of our duplex models. Instead, underthrusting in our models occurs only locally in response to individual horse blocks. The presence of a frontal buttress is a boundary condition necessary for large-scale underthrusting.

Next we asked what are the parameters controlling the duplex geometry (i.e. horse size and amount of displacement). Again the shortening rate or décollement strength appear to play a significant role. Under low shortening rates, the horse blocks are translated long distances, leading to flat-on-flat geometries. Under high shortening rates, flat-on-flat geometries are rare. Under low shortening rates, long (i.e. several tens of centimeters) thrust sheets can form, whereas high shortening rates lead to shorter thrust sheets (i.e. less than 10 cm).

Another question was whether or not certain types of structural features may be genetically related. Indeed, model results have evidenced specific associations of structural features that form systematically under similar boundary conditions. Active-roof duplexes that form under low shortening rates have the following attributes: (a) spaced culminations with large structural relief develop in the lower sand layer and are separated by broad synclines. (b)

The cover deformation is dominated by forethrusts located in-between the underlying culminations. The overall relief of the thrust wedge low. (c) The culminations tend to form antiformal stacks, although backthrusting in the lower layer is also common. (d) The thrust blocks are not internally deformed. (e) Significant layer-parallel bulk shortening (up to 10%) occurs. On the other hand, passive-roof duplexes formed under high shortening rates have the following attributes: (a) spaced ramp anticlines form. (b) The cover deforms by both folding and small fore- and backthrusting. (c) Backthrusting is less common in the lower layer. (d) Thrust blocks are internally deformed by small faults and box folds. (e) Layer-parallel bulk shortening is lower and occurs later. Furthermore, because the décollement becomes as strong or stronger than the underlying rock layers when the shortening rate is very high or the décollement highly viscous, no duplex forms, and the whole sequence folds. The folds may later be modified by thrust faults.

Finally, we asked what controls the timing of formation, growth and propagation of structures within a thrust duplex. Again the shortening rate and the décollement strength play a significant role. Under low shortening rates, an initial phase of layer-parallel shortening is followed by simultaneous formation of horse-block culminations. Horses within a single culmination may develop sequentially towards the foreland. Several out-of-sequence faults and folds develop within the cover and accommodate continued shortening in the underlying culminations. Under high shortening rates, the structures propagate sequentially towards the foreland and the amount of bulk shortening is small.

Acknowledgements

This research was supported by grants to Couzens-Schultz from Amoco, Arco and The Industrial Associates Program at the Center for Tectonophysics, Texas A&M University. The work represents a portion of the requirements for Couzens-Schultz's Ph.D. dissertation.

Appendix A. Model scaling and methods

Like other models (e.g. numerical or analytical), a physical model must be a replica of the natural prototype scaled-down in terms of dimensions, rheology, and boundary conditions (Hubbert, 1937; Ramberg 1981; Vendeville et al., 1987; Eisenstadt et al., 1995). Our thrust-belt models have a length ratio of about 10^{-5} (1 cm represents 1 km) so that thrust belts on the order of a few tens of kilometers wide and long, and 2–10 km thick can be simulated in the laboratory by models a few tens of centimeters wide and long and 2–10 cm thick. The experimental materials used to build the models include dry quartz sand and silicone polymers. These materials impose a density ratio of about 0.5 because their volumetric mass (900–1800 kg m^{-3}) is about half that of natural rocks (2000–2500 kg m^{-3}). Because experiments are run in a natural gravity field, rather than in a centrifuge, the gravity ratio will be unity. In order to properly scale the gravity stresses, the length ratio, L^*, gravity ratio, g^*, and density ratio, ρ^*, impose a stress ratio, σ^*, through the following relation:

$$\sigma^* = \rho^* g^* L^* \quad (1)$$

which requires the model-to-prototype ratio for stresses, σ^*, to be 5×10^{-6} (i.e. the model needs to be 200,000 times weaker than the prototype).

In the upper continental crust, brittle sedimentary rocks, such as the ones located in between décollement units, obey a Mohr–Coulomb criterion of failure, where the coefficient of internal friction is about 0.85 and the cohesion about 5×10^7 Pa (Byerlee, 1978). An analog material for brittle rocks should have a similar angle of internal friction, and because cohesion has dimensions of stresses, the analog material should have a cohesion about 5×10^{-6} times that of natural rocks (here, 250 Pa). The properties of dry quartz sand, as described by Krantz (1991) and by Schellart (2000), fulfill these scaling requirements to properly simulate brittle rocks (Table 2).

We used two Newtonian, viscous silicone polymers to simulate weak décollement layers in nature, such as evaporites or shales. The first polymer is RG20, a transparent polydimethylsiloxane (PDMS) manufactured by Rhone-Poulenc, US, and has a viscosity of about 1×10^4 Pa s. The second polymer, Silbione Silicone (a pink dilating compound manufactured by Rhône-Poulenc, France) has a viscosity of about 2×10^4 Pa s.

The natural analogs of the viscous décollement layers used in our experiments can be either (1) layers of viscous, evaporitic rocks, or (2) overpressured rocks having a frictional-plastic behavior that act as detachments. In the section below, we present how our models scale back to nature according to these two different hypotheses.

A.1. Viscous, evaporitic décollement layers in nature

In our experiments, we used variable displacement rates as a proxy for varying the viscosity of the décollement layer in nature. Because of their strain-rate dependence, viscous décollements are effectively stronger when deformed rapidly than when deformed slowly. Assuming a fixed rate of displacement (i.e. a rate of linear velocities in m s^{-1}) in nature (here, 1 cm $year^{-1}$), the model-to-prototype ratio for displacement rates, V^*, is:

$$V^* = V_{\text{model}}/V_{\text{nature}}, \quad (2)$$

where V_{model} is the linear velocity of the moving endwall in the experiment, and V_{nature} is the displacement rate of the backstop in nature.

Table 4
Scaling silicone as an overpressured frictional plastic detachment in nature

Length ratio	Silicone viscosity	Displacement rate (mm/h)	Displacement rate (m/s)	Décollement thickness (mm)	Décollement thickness (m)	Shear-strain rate (s^{-1})	Viscosity (model)	Shear strength (Pa) model	Shear stress without pressure $= \rho ghf$ (MPa)	Stress ratio	Equivalent shear stress in nature (MPa)	Equivalent overpressure in nature (%)	Coefficient of overpressure in nature (l)
1 cm = 1 km	Low viscosity	1	2.78×10^{-7}	2.5	0.0025	1.11×10^{-4}	1.00×10^{4}	1.11	41.69	5.00×10^{-6}	0.22	99.47	0.995
1 cm = 1 km	Low viscosity	5	1.39×10^{-6}	2.5	0.0025	5.56×10^{-4}	1.00×10^{4}	5.56	41.69	5.00×10^{-6}	1.11	97.33	0.973
1 cm = 1 km	Low viscosity	10	2.78×10^{-6}	2.5	0.0025	1.11×10^{-3}	1.00×10^{4}	1.11×10	41.69	5.00×10^{-6}	2.22	94.67	0.947
1 cm = 1 km	Low viscosity	50	1.39×10^{-5}	2.5	0.0025	5.56×10^{-3}	1.00×10^{4}	5.56×10	41.69	5.00×10^{-6}	11.11	73.35	0.733
1 cm = 1 km	Low viscosity	100	2.78×10^{-5}	2.5	0.0025	1.11×10^{-2}	1.00×10^{4}	1.11×10^{2}	41.69	5.00×10^{-6}	22.22	46.70	0.467
1 cm = 1 km	Low viscosity	500	1.39×10^{-4}	2.5	0.0025	5.56×10^{-2}	1.00×10^{4}	5.56×10^{2}	41.69	5.00×10^{-6}	111.11	−166.50	−1.665
1 cm = 1 km	High viscosity	1	2.78×10^{-7}	2.5	0.0025	1.11×10^{-4}	2.00×10^{4}	2.22	41.69	5.00×10^{-6}	0.44	98.93	0.989
1 cm = 1 km	High viscosity	5	1.39×10^{-6}	2.5	0.0025	5.56×10^{-4}	2.00×10^{4}	1.11×10	41.69	5.00×10^{-6}	2.22	94.67	0.947
1 cm = 1 km	High viscosity	10	2.78×10^{-6}	2.5	0.0025	1.11×10^{-3}	2.00×10^{4}	2.22×10	41.69	5.00×10^{-6}	4.44	89.34	0.893
1 cm = 1 km	High viscosity	50	1.39×10^{-5}	2.5	0.0025	5.56×10^{-3}	2.00×10^{4}	1.11×10^{2}	41.69	5.00×10^{-6}	22.22	46.70	0.467
1 cm = 1 km	High viscosity	100	2.78×10^{-5}	2.5	0.0025	1.11×10^{-2}	2.00×10^{4}	2.22×10^{2}	41.69	5.00×10^{-6}	44.44	−6.60	−0.066
1 cm = 1 km	High viscosity	500	1.39×10^{-4}	2.5	0.0025	5.56×10^{-2}	2.00×10^{4}	1.11×10^{3}	41.69	5.00×10^{-6}	222.22	−433.00	−4.330
1 cm = 2 km	Low viscosity	1	2.78×10^{-7}	2.5	0.0025	1.11×10^{-4}	1.00×10^{4}	1.11	83.39	2.50×10^{-6}	0.44	99.47	0.995
1 cm = 2 km	Low viscosity	5	1.39×10^{-6}	2.5	0.0025	5.56×10^{-4}	1.00×10^{4}	5.56	83.39	2.50×10^{-6}	2.22	97.33	0.973
1 cm = 2 km	Low viscosity	10	2.78×10^{-6}	2.5	0.0025	1.11×10^{-3}	1.00×10^{4}	1.11×10	83.39	2.50×10^{-6}	4.44	94.67	0.947
1 cm = 2 km	Low viscosity	50	1.39×10^{-5}	2.5	0.0025	5.56×10^{-3}	1.00×10^{4}	5.56×10	83.39	2.50×10^{-6}	22.22	73.35	0.733
1 cm = 2 km	Low viscosity	100	2.78×10^{-5}	2.5	0.0025	1.11×10^{-2}	1.00×10^{4}	1.11×10^{2}	83.39	2.50×10^{-6}	44.44	46.70	0.467
1 cm = 2 km	Low viscosity	500	1.39×10^{-4}	2.5	0.0025	5.56×10^{-2}	1.00×10^{4}	5.56×10^{2}	83.39	2.50×10^{-6}	222.22	−166.50	−1.665
1 cm = 2 km	High viscosity	1	2.78×10^{-7}	2.5	0.0025	1.11×10^{-4}	2.00×10^{4}	2.22	83.39	2.50×10^{-6}	0.89	98.93	0.989
1 cm = 2 km	High viscosity	5	1.39×10^{-6}	2.5	0.0025	5.56×10^{-4}	2.00×10^{4}	1.11×10	83.39	2.50×10^{-6}	4.44	94.67	0.947
1 cm = 2 km	High viscosity	10	2.78×10^{-6}	2.5	0.0025	1.11×10^{-3}	2.00×10^{4}	2.22×10	83.39	2.50×10^{-6}	8.89	89.34	0.893
1 cm = 2 km	High viscosity	50	1.39×10^{-5}	2.5	0.0025	5.56×10^{-3}	2.00×10^{4}	1.11×10^{2}	83.39	2.50×10^{-6}	44.44	46.70	0.467
1 cm = 2 km	High viscosity	100	2.78×10^{-5}	2.5	0.0025	1.11×10^{-2}	2.00×10^{4}	2.22×10^{2}	83.39	2.50×10^{-6}	88.89	−6.60	−0.066
1 cm = 2 km	High viscosity	500	1.39×10^{-4}	2.5	0.0025	5.56×10^{-2}	2.00×10^{4}	1.11×10^{3}	83.39	2.50×10^{-6}	444.44	−433.00	−4.330

Because the scaling ratio for linear velocities is related to the length and strain-rate ratios by the following equation:

$$V^* = L^* \times \epsilon^*, \quad (3)$$

the value for the strain rate ratio must be:

$$\epsilon^* = V^*/L^*, \quad (4)$$

which leads to the following value for the viscosity ratio:

$$\eta^* = \sigma^*/\epsilon^* = (\sigma^* L^*)/V^* \quad (5)$$

Table 3 lists the values for the equivalent viscosity of the natural décollement layer calculated for the two types of silicone polymer and the six displacement rates (ranging from 1 mm h^{-1} to 500 mm h^{-1}) used during the experiments. The lowest calculated value is 1.75' $\times 10^{17}$ Pa s and corresponds to models comprising a layer of RG20 polymer deformed at the lowest rate (1 mm h^{-1}). The highest value for natural viscosity is 1.75×10^{20} Pa s, corresponding to a layer of Silbione Silicone deformed at 500 mm h^{-1}.

Values between 1×10^{17} Pa s and 1×10^{19} Pa s fall into the range of viscosity values of evaporitic rocks in nature, such as halite or gypsum (Clark, 1966).

A.2. Frictional plastic detachment in nature

Assuming that the layers of viscous polymer in models represent strata of overpressured, frictional-plastic rocks in nature requires a different scaling approach that scales down the value of the shear stress in nature with that in models (Nalpas and Brun, 1993).

We first need to calculate the rate of horizontal shear strain, $\dot{\gamma}$, within the model's viscous décollement layer, assuming that deformation is evenly accommodated by shear of the entire décollement thickness:

$$\dot{\gamma} = V/H_{\text{model}} \quad (6)$$

where V is the displacement rate (in m s^{-1}) of the moving wall in experiments, and H_{model} is the thickness of the décollement (in m). Knowing the viscosity of the model's décollement layer, η_{model}, we can calculate the shear stress, τ (i.e. the shear strength) within the layer as follows:

$$\tau_{\text{model}} = \dot{\gamma}\,\eta_{\text{model}} \quad (7)$$

The equivalent value for shear stress in nature, τ_{nature}, can be calculated using the scale ratio for stresses, σ^*, which is already imposed by scaling of gravity forces (Eq. (1)). Hence:

$$\tau_{\text{nature}} = \tau_{\text{model}}/\sigma* \quad (8)$$

The final step consists of calculating the equivalent coefficient of overpressure in nature, λ, based on the following equation described in Hubbert and Rubey (1959):

$$\tau_{\text{nature}} = \rho_{\text{nature}} g H_{\text{nature}} f(1 - \lambda) \quad (9)$$

where ρ_{nature} is the volumetric mass of natural rocks (here, chosen as 2500 kg m^{-3}), H_{nature} is the thickness of the cover (here, about 2000 m), f is the coefficient of internal friction of the rocks forming the detachment (here, 0.85), and λ is the coefficient of overpressure.

Table 4 illustrates the values of the coefficient of overpressure, λ, for each type of silicone décollement and displacement rate. Except for the two fastest experiments (deformed under 500 m h^{-1}), the predicted values range between very high (>0.99, corresponding to the weakest silicone polymer deformed at 1 mm h^{-1}) to negligible (e.g. for the strongest silicone polymer deformed at 100 mm h^{-1}). For the two highest displacement rates, the predicted strength of the detachment actually equals or exceeds that of the cover rocks and would therefore correspond to the case of an abnormally strong detachment. However, because the values for shear stresses in both model and nature were calculated assuming that in the entire model the cover advance at the same displacement rate as that of the backstop, these values represent maximum estimates. As the cover internally deforms, only the cover located immediately against the backstop moves at the same rate. Farther from the backstop, the cover advances more slowly, therefore the associated basal shear stress can be considerably lower.

References

Banks, C.J., Warburton, J., 1986. 'Passive-roof' duplex geometry in the frontal structures of the Kirthar and Sulaiman mountain belts, Pakistan. Journal of Structural Geology 3, 229–238.

Belotti, H.J., Saccavino, L.L., Schachner, G.A., 1995. Structural styles and petroleum occurence in the Sub-Andean thrust belt of northern Argentina. In: Tankard, A.J., Suárez S., Welsink, H.J. (Eds.), Petroleum Basins of South America. American Association of Petroleum Geologists Memoir 62, pp. 545–555.

Boyer, S.E., 1992. Geometric evidence for synchronous thrusting in southern Alberta and northwest Montana thrust belts. In: McClay, K.R., (Ed.), Thrust Tectonics, Chapman and Hall, London, pp. 377–390.

Boyer, S.E., Elliott, D., 1982. Thrust systems. American Association of Petroleum Geologists Bulletin 66, 1196–1230.

Byerlee, J.D., 1978. Friction of rocks. Pure and Applied Geophysics 116, 615–626.

Clark, G.B., 1966. Deformation moduli of rocks. In: Testing Techniques for Rock Mechanics—ASTM 5th Pacific Area National Meeting, Seattle. American Society for Testing and Materials Special Technical Publication 402, pp. 133–172.

Costa, E., Vendeville, B.C., 2002. Experimental insights on the geometry and kinematics of fold-and-thrust belts above weak, viscous evaporitic décollement. Journal of Structural Geology 24, 1729–1739.

Couzens-Schultz, B.A., 1997. The Effects of Mechanical Stratigraphy on the Origin of Triangle Zones in Thrust Belts. Ph.D. dissertation, Texas A&M University, College Station, TX.

Dahlen, F.A., Suppe, J., Davis, D., 1984. Mechanics of fold-and-thrust belts and accretionary wedges: cohesive Coulomb theory. Journal of Geophysical Research 89, 10087–10101.

Davies, R.K., Fletcher, R.C., 1990. Shear bands in a plastic layer at yield under combined shortening and shear: a model for the fault array in a duplex. In: Knipe, R.J., Rutter, E.H. (Eds.), Deformation Mechanisms, Rheology and Tectonics. Geological Society of London Special Publication 54, pp. 123–132.

Eisenstadt, G., Vendeville, B.C., Withjack, M.O., 1995. Introduction to

Experimental Modeling of Tectonic Processes. Continuing Education Course Notes, Geological Society of America, unpaginated.

Erickson, S.G., 1995. Mechanics of triangle zones and passive-roof duplexes: implications of finite element models. Tectonophysics 245, 1–11.

Harrison, J.C., 1993. Salt involved tectonics of a foreland folded belt, Arctic Canada. In: American Association of Petroleum Geologists Hedberg Conference on Salt Tectonics, Bath, England, pp. 13–17.

Hubbert, M.K., 1937. Theory of scale models as applied to the study of geologic structures. Geological Society of America Bulletin 70, 115–205.

Hubbert, M.K., Rubey, W., 1959. Role of fluid pressure in mechanics of over-thrust faulting. Geological Society of America Bulletin 48, 1459–1519.

Jamison, W.R., 1993. Mechanical stability of the triangle zone: the backthrust wedge. Journal of Geophysical Research 98, 20,015–20, 030.

Jamison, W.R., 1996. Mechanical models of triangle zone evolution. Bulletin of Canadian Petroleum Geology 44, 180–194.

Jones, P.B., 1996. Triangle zone geometry, terminology and kinematics. Bulletin of Canadian Petroleum Geology 44, 139–152.

Krantz, R.W., 1991. Measurements of friction coefficients and cohesion for faulting and fault reactivation in laboratory models using sand and sand mixtures. Tectonophysics 188, 203–207.

Kulander, B.R., Dean, S.L., 1986. Structure and tectonics of southern and central Appalachian Valley and Ridge Plateau Provinces. West Virginia and Virginia. American Association of Petroleum Geologists Bulletin 70, 1674–1684.

Lebel, D., Langenberg, W., Mountjoy, E.W., 1996. Structure of the central Canadian Cordilleran thrust-and-fold belt, Athabasca-Brazeau area, Alberta: a large, complex intercutaneous wedge. Bulletin of Canadian Petroleum Geology 44, 282–298.

MacKay, P.A., Spratt, D.A., Soule, G.S., Lawton, D.C., 1994. The triangle zone of southern Alberta—geometry, lateral variations and associated oil and gas fields. Fieldtrip Guidebook Canadian Society of Economic Geologists/Canadian Society of Petroleum Geologists Convention, Calgary, Alberta.

McClay, K.R., 1992. Glossary of thrust tectonic terms. In: McClay, K.R., (Ed.), Thrust Tectonics, Chapman and Hall, London, pp. 419–434.

Mugnier, J.L., Baby, P., Colletta, B., Vinour, P., Bale, P., Leturmy, P., 1997. Thrust geometry controlled by erosion and sedimentation: a view from analogue models. Geology 25, 427–430.

Nalpas, T., Brun, J.-P., 1993. Salt flow and diapirism related to extension at crustal scale. Tectonophysics 228, 349–362.

Price, R.A., 1986. The southeastern Canadian Cordillera: thrust faulting, tectonic wedging, and delamination of the lithosphere. Journal of Structural Geology 3, 239–254.

Ramberg, H., 1981. Gravity, Deformation and the Earth's Crust, Academic Press, London.

Schellart, W.P., 2000. Shear test results for cohesion and friction coefficients for different granular materials: scaling implications for their usage in analogue modelling. Tectonophysics 324, 1–16.

Smart, K.J., Couzens-Schultz, B.A., 2001. Mechanics of blind foreland thrusting: comparison of numerical and physical modeling. Journal of Geology 109, 771–779.

Soule, G.S., Spratt, D.A., 1996. En échelon geometry and two-dimensional model of the triangle zone, Grease Creek syncline area, Alberta. Bulletin of Canadian Petroleum Geology 44, 244–257.

Vendeville, B., Cobbold, P.R., Davy, P., Choukroune, P., Brun, J.P., 1987. Physical models of extensional tectonics at various scales. In: Coward, M.P., Dewey, J.F., Hancock, P.L. (Eds.), Continental Extensional Tectonics. Geological Society of London Special Publication 28, pp. 98–108.

Vergés, J., Martínez, A., 1988. Corte Compensado del Pirineo oriental: geometria de las cuencas de antepais y edades de emplazamiento de los mantos de corrimiento. Acta Geológica Hispánica 23, 95–106.

Wallace, W.K., 1993. Detachment folds and a passive-roof duplex: examples from the northeastern Brooks Range, Alaska. In: Solie, D.N., Tannian, F. (Eds.), Short Notes on Alaskan Geology. Alaska Division of Geological and Geophysical Surveys Geologic Report 113, pp. 81–99.

Williams, W.D., Dixon, J.S., 1985. Seismic interpretation of the Wyoming overthrust belt. In: Gries, R.R., Dyer, R.C. (Eds.), Seismic Exploration of Rocky Mountain Region, Rocky Mountain Association of Geology, Denver, Colorado, pp. 13–22.

Willis, B., 1893. The mechanics of Appalachian Structure. U.S. Geological Survey Annual Report 13 (1891–1892), part 2, pp. 217–281.

Wilson, T.H., Schumaker, R.C., 1992. Three-dimensional structural interrelationships within Cambro-Ordovician lithotectonic unit of the central Appalachians. American Association of Petroleum Geologists Bulletin 74, 1310–1324.

Woodward, N.B., 1985. Valley and Ridge thrust belt: balanced structural sections, Pennsylvania to Alabama. University of Tennessee, Department of Geological Sciences, Studies in Geology 12, Knoxville, Tennessee.